# Multiscale modeling of concrete and of the FRP-concrete interface

V. Palmieri[1], L. De Lorenzis[2]

[1] *Dipartimento di Ingegneria dell'Innovazione, Università del Salento, via per Monteroni, 73100 Lecce, Italy.*

[2] *Corresponding Author. Institut für Angewandte Mechanik, Technische Universität Braunschweig, Bienroder Weg 87, 38106 Braunschweig, Germany.*

**Abstract**

Cracking and failure processes in concrete members as well as debonding mechanisms between concrete surfaces and fiber-reinforced polymer composites used for structural strengthening are often modeled through macroscopic empirically-based cohesive zone models. This approach presents a number of limitations, as macroscopic laws spatially homogenize complex damage and failure processes taking place at the lower scales. This paper proposes a multiscale approach for concrete and for the determination of mixed-mode cohesive zone models for the composite-concrete interface based on mesomechanical analysis. The mesomechanical model includes the explicit description of the heterogeneous material geometry close to the interfacial zone, as well as a continuum damage description for both the cement matrix and the matrix-aggregate interfacial transition zone. Macroscopic mixed-mode cohesive zone laws are then obtained through a numerical homogenization procedure. The choice of the representative volume element is discussed and the cohesive behavior under mode-I, mode-II and loading conditions with different degrees of mode mixity is analyzed. Comparisons with available experimental and analytical results are also performed.

*Keywords:* concrete, cohesive zone model, FRP-concrete bond, homogenization, mesomechanical modeling, mixed-mode fracture, multiscale modeling.

## 1. INTRODUCTION

The concept of the cohesive zone model (CZM), usually implemented in the framework of the finite element (FE) method, has been widely used to analyze fracture problems both within a single material and at bimaterial interfaces in a number of material systems including concrete, polymers, metals, ceramics, and several types of composites such as fiber reinforced polymers (FRP) (Xu and Needleman 1994, Tvergaard and Hutchinson 1992, Camacho and Ortiz 1996, Geubelle and Baylor 1998). CZM approaches have been used to simulate fracture under static, dynamic, and cyclic loading conditions (Camacho and Ortiz 1996, Xu and Needleman 1994), delamination of layered composites (Pantano and Averill 2004), debonding of FRP sheets from concrete, masonry or steel substrates (Chen and Teng 2001, De Lorenzis and Zavarise 2009), or to describe the macroscopic constitutive behaviour of a thin adhesive layer (Li et al. 2006).

Early cohesive failure models were developed for the mode-I fracture process, relating normal traction and separation. The CZM was later extended to the mode-II fracture process, in which the tangential traction and separation are considered instead. Experimental observations show distinctive characteristics of the micromechanical failure mechanisms in peel and shear fracture, thus the cohesive behaviour is expected to be mode-dependent (Roy et al. 1999, Chai 2003). At the meso- or microscale of observation, interfacial fracture nearly always involves mixed-mode conditions. Also, macroscopic mixed-mode conditions take place at a variety of bonded interfaces existing in practice, such as in various types of lap joints (Kafkalidis and Thouless 2002), and at the interface between FRP and concrete or steel substrate in the proximity of inclined cracks or at the edge of the FRP plate (Yao et al. 2005, Pan and Leung 2007, De Lorenzis et al. 2013). Mode mixity also affects interfacial debonding between a thin plate and a curved substrate, which is relevant to the structural analysis of FRP-strengthened concrete beams with curved soffits or masonry arches (De Lorenzis 2012).

Different approaches have been used for the numerical modeling of interfaces under mixed-mode conditions, including the uncoupled and the coupled CZM approaches. In the latter case, the mode-I and

mode-II cohesive laws may or may not be derived from a potential (De Lorenzis and Zavarise 2008). In any case, the vast majority of the available CZM formulations are purely phenomenological, and "lump" all the micromechanical processes occurring within the fracture process zone. Obviously, these processes vary widely depending on the type of material, geometry and loading conditions. A CZM of this type, based on macro-scale phenomenology, spatially homogenizes all effects that occur at the interface, which demands caution when comparing the cohesive zone (CZ) parameters with experiments. A good example was provided by Hoefnagels et al. (2010) while applying CZ modeling to the copper-rubber interface in stretchable electronics. They found that the calibrated parameters of the chosen macro-scale CZ law varied by orders of magnitude as the experimental setup was changed. For the above reasons, any macroscopic phenomenological CZM calibrated for a certain geometry and test setup is not necessarily applicable to simulate the same interface under different loading conditions or substrate thicknesses.

In this paper, attention is focused on the interface between FRP sheets and concrete. Concrete has a highly heterogeneous microstructure and several numerical micromechanics analyses of the interaction between its various components have been developed to deduce its macroscopic constitutive behaviour (see the brief review in Section 2.1). Despite fracture in concrete having been extensively interpreted with CZMs, there have been very limited attempts to derive the shape and magnitude of the cohesive law based on a detailed consideration of the microstructure. Considering the case of FRP sheets bonded to concrete substrates, interfacial failure typically occurs by formation of a crack within the concrete, a few millimeters from the bond line, and is thus heavily influenced by the heterogeneous nature of the concrete superficial layer. The interfacial behavior is often described with CZMs. Several phenomenological CZMs are available for the FRP-concrete interface in macroscopic mode II, and in many cases the bilinear shape is adopted showing generally a satisfactory correlation with test results (Chen and Teng 2001). However, these models are unable to interpret the competition between different cohesive crack paths based on the micromechanical details of the substrate. Moreover, they cannot deal with mixed-mode loading. Very limited investigations have focused on such interfaces under mixed-mode conditions which very often result from geometry, loading and/or deformation-induced effects (De Lorenzis and Zavarise 2008, Karbhari et al. 1997, Wan et al. 2004). They have pointed out a complex influence of the mode mixity on the microstructural details of the failure mechanism and on the consequent strength of the interface (Karbhari et al. 1997). The same considerations about case-sensitivity of macroscopic phenomenological CZMs apply of course to this type of interface, whose modeling is particularly challenging due to the complexity of the microstructure.

A solution to the above issues can be found by accounting explicitly for the processes occurring at the lower scales, and transferring these informations to the macroscale in a consistent manner, which is the idea underlying multiscale approaches. In the case of continuum models, numerical homogenization is based on computationally averaging the generated microstructural stress and deformation over a representative volume element (RVE), thereby implicitly establishing an effective constitutive relation between the average stress and deformation. Over the past two decades, various approaches have been developed along this line (see Zohdi and Wriggers 2001 for a review, with further more recent contributions including Kouznetsova et al., 2001, Miehe and Koch, 2002, Pelissou et al., 2009, among many others). These approaches rely on a local periodicity of the microstructure in the direct neighborhood of the RVE, but do not require global periodicity.

Numerical homogenization frameworks for thin layer problems are much more recent and focused thus far on heterogeneous adhesive layers. In Matouš et al. (2008) and Kulkarni et al. (2009) a mesoscale CZM formulation was derived from numerically homogenizing the microscale failure processes in a thin, heterogeneous adhesive, as simulated with an isotropic damage model. The examples presented therein involved only a one-way coupling between the scales by specifying an arbitrary macroscopic displacement jump across the heterogeneous adhesive layer and extracting the corresponding macroscopic tractions through the computational homogenization approach. In Hirschberger et al. (2009), the multi-scale cohesive scheme of Matouš et al. (2008) was extended to the case of finite deformations. However, this work did not involve modeling of failure or softening at the macro- and micro-levels. In Kulkarni et al. (2010) the first steps were made towards the multi-scale modeling of structures with heterogeneous interfaces involving a two-way coupling between the macro- and micro-scales. This work considers the situation of an adhesive layer with embedded perfectly bonded particles. Cid Alfaro et al. (2010) also focuses on the derivation of a mesoscale cohesive zone model from the numerical homogenization of microscale fracture processes in a thin layer. The homogenization framework developed here shows similarities with that of Geubelle and co-workers. However, the microscale fracture processes are modeled with the CZM approach rather than in a smeared

fashion using a continuum damage model. Although the homogenization framework presented is applicable to arbitrary, mixed-mode loading conditions, the numerical examples focus upon uniaxial tension. Verhoosel et al. (2010) also proposed an averaging scheme that provides traction-opening relations governing the evolution of macroscopic cracks. In the case of a crack running within the bulk of the material, the averaging relations are applied to an FE model representing the material in the vicinity of the crack. In the case of a crack at a bimaterial interface within the domain, the employed microscale model represents the material in the adhesive layer. Since for both cases the obtained macroscopic traction-opening relations are only defined on macroscopic cracks, the proposed averaging scheme can be regarded as a homogenization procedure applied along the macroscopic cracks.

This paper describes a numerical homogenization procedure applied to concrete and to the FRP-concrete interface. The focus here is on the so-called mesoscale, where the coarser aggregates are explicitly described and the finer aggregates are incorporated in the matrix (mortar) behavior. The main idea is the determination of macroscopic mixed-mode CZ laws for the FRP-concrete interface through numerical homogenization of the mesoscale behavior, whereby the three involved constituent phases (aggregates, matrix and aggregate-matrix interface) are mechanically modeled with appropriate constitutive laws. A mesomechanical testing procedure and a meso-macroscale transition are then devised to derive macroscopic CZ laws based on mesostructural details. Note that, although this work had FRP-concrete bond as primary motivation, the presented approach is equally well applicable to other interface regions in concrete structures, as well as to interfaces in other quasi-brittle materials (provided that the respective geometry features and material behavior are properly accounted for).

The paper is organized as follows. Section 2 illustrates the mesomechanical modeling of the concrete, including numerical generation of the aggregate geometry and constitutive modeling of the involved constituent phases. The developed model is applied to three benchmark tests, involving uniaxial tension and uniaxial compression of concrete specimens, as well as a classical FRP-concrete bond test. The first two tests are used to calibrate reasonable values of the unknown parameters in the constitutive models, whereas results of the third test are compared with experimental values. Section 3 develops the mesomechanical formulation to study the behaviour of the FRP-concrete interface. The meso-macroscale transition is derived herein based on Hill's energy consistency condition. In Section 4, the choice of the representative volume element (RVE) is first discussed. Subsequently, CZ macroscopic laws are derived in mode-I, mode-II and mixed-mode loading conditions and several relevant observations are set forth. Also, a comparison with phenomenological analytical models from the literature is performed. Finally, Section 5 summarizes the main conclusions.

## 2. MESOMECHANICAL MODEL FOR CONCRETE

The multiscale approach sought in this work requires the explicit definition of the mesostructure of the interface between FRP sheets and concrete, i.e. of the superficial layer of concrete in the vicinity of the bondline. Therefore, a necessary intermediate step is the development of a mesomechanical model for concrete, which is illustrated in this section. After a brief literature review, the algorithm adopted for the description of the geometry and the material modeling approach are presented. Subsequently, the choice of the discretization and simulation parameters is motivated and mesh sensitivity issues associated with local damage modeling are discussed. Finally, benchmark tests on concrete numerical specimens are performed. These include tensile and compression tests, as well as FRP-concrete bond tests. In the latter case, a comparison with available experimental results is also presented.

### *2.1. Previous work*

Several mesomechanical models have been developed to study the damage and failure mechanisms of concrete and other quasi-brittle heterogeneous materials. Many early models were based on idealized mesostructures (random particle model, Bažant et al. 1990, framework model, Schorn and Rode 1991, and lattice model, Schlangen and van Mier 1992). They replace the continuous constituents (coarse aggregate, matrix and interface zones) with one-dimensional discrete elements featuring non-linear stress-strain relationships. Other early models were already based on a more realistic description of the mesoscale geometry (Wittmann et al. 1984, De Schutter and Taerwe 1993), with coarse aggregates and matrix modeled with two-dimensional finite elements.

More recent models are mostly based on the latter approach, and typically consider concrete as a three-phase composite including mortar, coarse aggregate and the interfacial transition zone (Wang et al. 1999, Teng et al. 2004, Zhu et al. 2004, Häfner et al. 2006, Snozzi et al. 2011). These models mainly differ from each other in the representation of the geometry, in the method used to characterise the randomness and heterogeneity of concrete at the mesolevel, as well as in the material models used for the single phases. The method for the geometry description ranges from hand drawing (Zhu et al. 2004) to Voronoi tessellation (Snozzi et al. 2011) to ad-hoc elaborated procedures incorporating random variables (Wang et al. 1999). The material models include rotating crack, damage and CZ approaches. In spite of the differences, all these models share the objective of deriving the macroscopic mechanical response of concrete from the detailed consideration of the meso-level geometry and material behavior. This is obviously a simplified view which neglects lower-scale effects such as the role of the finer aggregates and the multiscale nature of the cement paste, but seems to be the most viable option at the current stage. The vast majority of the previous studies considered a 2D geometry, which is a rather crude assumption but maintains the computational effort within reasonable limits. 3D approaches have been proposed by Caballero et al. (2006) and Wriggers and Moftah (2006). In this paper, we limit ourselves to a 2D geometry.

### *2.2. Definition of the geometry*

The concrete mesostructure is here intended as being constituted by the coarse aggregates, the cement paste with the finer aggregates embedded, and the interfacial transition zone (ITZ) between coarse aggregates and paste. For the generation of the mesostructure, several studies are available based on different criteria and procedures. An important distinction is based on the shape of the coarse aggregates, which is generally taken as round or angular for gravel or crushed rock types, respectively. This paper considers concrete made with crushed rock aggregates, for which the procedure proposed by Wang et al. (1999) for the numerical generation of a random aggregate structure of angular shape is adopted. The main steps involved are summarized as follows, while further details can be retrieved in the original paper.

#### *2.2.1. Grading curve and outline of the procedure*

First of all, a suitable grading curve must be selected. This is given as a function $P(D)$, which represents the cumulative percentage of aggregate $P$ passing through the sieve of aperture size $D$. The latter ranges between $D_{min}$ and $D_{max}$, which coincide respectively with the minimum and maximum size of the coarse aggregate. Herein, the classical Fuller curve is adopted, i.e.

$$P = 100\sqrt{\frac{D}{D_{max}}} \tag{1}$$

Once $P(D)$ is known, the area of aggregate contained within the $i^{th}$ of the $s$ grading segments, $[D_i, D_{i+1}]$, can be computed as

$$A_{agg,i} = \frac{P(D_i) - P(D_{i-1})}{P(D_{max}) - P(D_{min})} A_{agg} \tag{2}$$

where $A_{agg}$ is the total area of coarse aggregates, in turn equal to a desired fraction $R_{agg}$ of the total concrete area, ranging for most concretes between 0.4 and 0.5.

The generation of the aggregate structure proceeds through a take-and-place process, which is conducted for each grading segment starting with the largest one and proceeding until the smallest. For the generic segment $i$, once its aggregate area $A_{agg,i}$ is computed with eq. (2), a number of particles of random shape and size are generated (take process) and placed (place process) into the area of the concrete specimen, until the area of aggregate left to be generated is insufficient for the creation of an additional particle within the same grading segment. When this condition is reached, the remaining aggregate area is added to the next grading segment and the procedure continues for this segment.

#### *2.2.2. The take process*

In the take process, the aggregate particles are generated as randomly shaped polygons, with size (i.e. width) dictated by the current grading segment and elongation (i.e. length to width ratio) prescribed as a random variable uniformly distributed between two predetermined values $\lambda_{min}$ and $\lambda_{max}$. These values must

be chosen upfront, possibly based on observations of the real aggregate geometry. In this study it is $\lambda_{min} = 1$ and $\lambda_{max} = 3$.

The shape of a polygon is completely defined by the number of sides $n$, and by the polar radii $r_j$ and the polar angles $\theta_j$ of the $n$ vertices. Following visual observations and in line with Wang et al. (1999), $n$ is taken herein as a random integer variable uniformly distributed between 4 and 10. The polar radii $r_j$ are also considered as uniformly distributed random variables in the range between $r_{min}$ and $r_{max}$, whereas the polar angles are found by first computing the angles subtended by consecutive sides, $\phi_j = \theta_{j+1} - \theta_j$. The latter are taken as random variables, uniformly distributed with an average value $2\pi/n$ and assumed to differ from this average by a maximum of $\delta 2\pi/n$, with a predetermined value of $\delta \leq 1$. The subtended angles obtained from the random procedure are normalized to ensure that their sum equals $2\pi$, as follows

$$\tilde{\phi}_j = \frac{2\pi}{\sum_k \phi_k} \phi_j \tag{3}$$

and the polar angles are subsequently evaluated as

$$\theta_j = \beta + \sum_{k=1}^{j-1} \tilde{\phi}_k \tag{4}$$

where $\beta$ is a phase angle determining the orientation of the particle, also obtained from a random uniform distribution.

Each particle as it results from the random generation procedure features a size and an elongation that do not necessarily correspond to the desired values. As in Wang et al. (1999), the size is herein assumed to coincide with the width of the particle, and the latter is computed as the minimum width of a rectangle excribing the particle, which is consistent with the meaning of variable $D$ as the aperture size of a sieve. Also, the elongation is obtained as the length to width ratio of the minimum-width rectangle. Once the actual width and elongation of the particle are computed, straightforward scalings can be implemented to bring them to the desired values.

#### *2.2.3. The place process*

Once a particle is generated, its positioning within the concrete specimen requires that the coordinates of a reference point and the orientation angle $\beta$ be specified. These three quantities are also considered as random variables, whereby the first two vary within the area of the concrete specimen and the last one between 0 and $2\pi$. Also, it is assumed that each particle is surrounded by a mortar layer of thickness $\gamma$ times the particle size. The value of $\gamma$ is assumed to vary between $\gamma_{min}$ and $\gamma_{max}$. In this study, we take $\gamma_{min} = 0.05$ and $\gamma_{max} = 0.15$.

### *2.3. Material modeling*

In this work, the aggregates are considered linearly elastic, whereas both the cement matrix and the ITZ are modeled with the isotropic damage law by Mazars (Pijaudier-Cabot and Mazars 2001). The main features of the damage model are briefly summarized as follows.

The isotropic damage model by Mazars adopts a single scalar damage variable $d$, ranging from 0 for the undamaged state to 1 for the fully damaged state. Thus the stress-strain relation reads

$$\varepsilon_{ij} = \frac{1+\nu_0}{E_0(1-d)}\sigma_{ij} - \frac{\nu_0}{E_0(1-d)}\sigma_{kk}\delta_{ij} \tag{5}$$

where $E_0$ and $\nu_0$ are respectively the elastic modulus and the Poisson's ratio of the undamaged material, $\sigma_{ij}$ and $\varepsilon_{ij}$ are the components of the stress and strain tensors, and $\delta_{ij}$ is Kronecker's delta. The damage variable is evaluated from an appropriate combination of tension and compression damage, as follows

$$d = \alpha_t d_t + \alpha_c d_c \tag{6}$$

where $d_t$ and $d_c$ are the damage variables in tension and compression, respectively, combined through the weigthing coefficients $\alpha_t$ and $\alpha_c$.

The computation of the weighting coefficients is summarized as follows, see Pijaudier-Cabot and Mazars (2001) for more details. The first step is the decomposition of the stress tensor (expressed in principal coordinates) into a positive and a negative part

$$\boldsymbol{\sigma} = \langle \boldsymbol{\sigma} \rangle_+ + \langle \boldsymbol{\sigma} \rangle_-$$

where $\langle \boldsymbol{\sigma} \rangle_+$ contains the positive and $\langle \boldsymbol{\sigma} \rangle_-$ the negative stress eigenvalues. More in detail, $\langle \sigma_a \rangle_+ = \sigma_a$ if $\sigma_a \geq 0$, $\langle \sigma_a \rangle_+ = 0$ if $\sigma_a < 0$, and $\langle \sigma_a \rangle_- = -\langle -\sigma_a \rangle_+$, with $\sigma_a$ as the principal stresses. From the stress decomposition, a strain decomposition is obtained as follows

$$\boldsymbol{\varepsilon}_t = \frac{1+\nu_0}{E_0} \langle \boldsymbol{\sigma} \rangle_+ - \frac{\nu_0}{E_0} tr \langle \boldsymbol{\sigma} \rangle_+ \tag{7}$$

$$\boldsymbol{\varepsilon}_c = \frac{1+\nu_0}{E_0} \langle \boldsymbol{\sigma} \rangle_- - \frac{\nu_0}{E_0} tr \langle \boldsymbol{\sigma} \rangle_- \tag{8}$$

Finally, the weigthing coefficients are derived from

$$\alpha_t = \sum_{a=1}^{3} H_a \frac{\varepsilon_{ta} (\varepsilon_{ta} + \varepsilon_{ca})}{\tilde{\varepsilon}^2} \tag{9}$$

$$\alpha_c = \sum_{a=1}^{3} H_a \frac{\varepsilon_{ca} (\varepsilon_{ta} + \varepsilon_{ca})}{\tilde{\varepsilon}^2} \tag{10}$$

where $\varepsilon_a = \varepsilon_{ta} + \varepsilon_{ca}$ are the principal strains, $H_a = 1$ if $\varepsilon_a \geq 0$ and $H_a = 0$ if $\varepsilon_a < 0$, and the equivalent strain $\tilde{\varepsilon}$ is defined as

$$\tilde{\varepsilon} = \sqrt{\sum_{a=1}^{3} (\langle \varepsilon_a \rangle_+)^2} \tag{11}$$

with the same meaning of the "positive" Macauley brackets $\langle \varepsilon_a \rangle_+$ illustrated above.

The damage variables in tension and compression evolve based on the following relationships

$$d_t = 1 - \frac{k_0(1-A_t)}{\tilde{\varepsilon}} - \frac{A_t}{exp[B_t(\tilde{\varepsilon} - k_0)]} \tag{12}$$

$$d_c = 1 - \frac{k_0(1-A_c)}{\tilde{\varepsilon}} - \frac{A_c}{exp[B_c(\tilde{\varepsilon} - k_0)]} \tag{13}$$

As can be inferred from eqs. (5), (12) and (13), this material model requires 7 parameters: $E_0$, $\nu_0$, $k_0$, $A_t$, $B_t$, $A_c$, $B_c$. Beside $E_0$ and $\nu_0$ whose meaning is clear, $k_0$ can be set as the strain at peak stress of the material under uniaxial tension, i.e.

$$k_0 = \frac{f_t}{E_0} \tag{14}$$

where $f_t$ is the material tensile strength.

In the present 2D implementation, plane stress conditions are assumed. Within a 2D approximation of the aggregate geometry, plane stress conditions are believed to be more appropriate as they correspond to simulating a concrete specimen of small thickness. In such a case it is reasonable that the aggregate geometry be constant across the thickness. Conversely, plane strain conditions imply a large out-of-plane thickness which contradicts the 2D nature of the aggregate geometry.

### *2.4. Discretization and choice of simulation parameters*

The concrete geometry was created with the procedure outlined in Sect. 2.2. The set of geometry parameters used in this investigation is reported in Table 1. Figure 1 shows three sample geometries obtained with different aggregate ratios. This geometry was then automatically meshed with triangular linear elements using the advancing front technique. Matching meshes for aggregate and mortar were obtained. The constitutive properties of the ITZ were assigned to the first layer of elements around each aggregate (Figure 2).

As a preliminary step to the actual simulations on concrete specimens, tensile and compression tests were run on matrix square specimens with 300-mm side, of which only a quarter were modeled exploiting symmetry conditions. The properties of the material are reported in Table 1. These tests were used to calibrate the optimal pseudo-time step to be used in the analyses, as well as to quantify the well-known mesh sensitivity effect associated to local damage models. The optimal pseudo-time step was chosen as the maximum value for which a mesh with 2 elements reproduced the analytical behavior with satisfactory accuracy, as shown in Figures 3a,c. Note that the analytical behavior was straightforwardly obtained from the model in Section 2.3 specialized for a uniaxial case. Regarding the mesh sensitivity issue, Figures 3b,d show the tensile and compressive stress-strain curves obtained from different meshes. As expected, mesh refinement leads to an earlier and increasingly abrupt decrease of the stress after the peak, due to strain localization. This effect seems to saturate for elements smaller than a given maximum size. This size was thus set as an upper bound for the meshes used in all subsequent simulations, in order to mitigate mesh sensitivity effects. The same phenomenon can be circumvented by using e.g. the crack band theory by Bažant and Oh (1983), or more sophisticated damage models such as non-local or strain-gradient models. These may be considered for extensions of the present study.

### *2.5. Benchmarking*

#### *2.5.1. Uniaxial tension and compression*

Before being used for modeling the FRP-concrete interface, the mesomechanical concrete model described in the previous section was tested under simple loading conditions, i.e. uniaxial tension and uniaxial compression. For both tests, a square concrete specimen with 300-mm size was used, a quarter of which was modeled exploiting symmetry (Figure 4).

As mentioned in the previous section, local damage models are well known to suffer from mesh sensitivity induced by strain localization. To circumvent this problem, non-local or gradient enhancements of the model or the use of the crack band approach are needed and will be pursued in future developments. Herein, these effects were mitigated on one side by an appropriate choice of the maximum element size (see Section 2.4), on the other side by the heterogeneous nature of the sample which to some extent dictates the range of feasible discretizations and mitigates the occurrence of localization. For the heterogeneous concrete specimen as opposed to a homogeneous one, the size of the element has an upper bound equal to the minimum distance between aggregates. Moreover, for consistency of the multiscale procedure, the lower bound of the element size should be set as the maximum characteristic length of the lower scale, e.g. the size of the small aggregates which are considered dispersed in the mortar.

Table 1 summarizes the material parameters adopted in the present investigation for the three phases. The stress-strain curves obtained from uniaxial tensile and compressive tests are reported in Figure 5. Figure 5a illustrates the tensile stress-strain response for concrete specimens with different aggregate ratios (including the limit case of no aggregates for comparison purposes) and with only two phases (i.e. matrix and aggregates). The presence of the aggregates, as expected, leads to a larger initial stiffness, which increases with the aggregate ratio. On the other hand, the tensile strength of the specimen decreases below the value of the matrix due to the local stress concentrations generated by the angular aggregates, and is not significantly influenced by the aggregate ratio. A similarly moderate influence of the aggregate ratio on the response has been reported by Lopez et al. (2008) and Zhu et al. (2004). The fact that the matrix with aggregates is predicted to be more brittle than the pure matrix appears rather unrealistic, but is a direct consequence of the adopted damage model. Future enhancements of the model should overcome this drawback.

Considering the presence of the ITZ with a strain at peak stress $k_0$ lower than the matrix (Table 1), the tensile strength decreases whereas the other behavioral features remain nearly unchanged (Figure 5b). Figures 5c,d report analogous results under compression.

Figures 6 and 7 display the evolution of the damage variable distribution during the tension and the compression tests, respectively. Under tension, damage is seen to start close to the peak stress mostly within the ITZ and to propagate gradually along the direction perpendicular to the applied load during the softening stage. In the advanced softening region, the damage pattern closely resembles the shape of a crack running through the specimen in a nearly horizontal direction, which agrees with intuition and with the experimental evidence. Under compression, a significant damage accumulation starts already during the increasing branch of the stress-strain response. Once again, at the advanced softening stage the damage contour assumes a complex and diffuse pattern along crossed inclined directions which resembles the cracking patterns usually obtained experimentally.

*2.5.2. FRP-concrete bond test*

As a further benchmark, a classical FRP-concrete bond test was simulated using the mesomechanical concrete model. The specimen consists of a concrete prism bonded with an FRP strip, whose geometry and boundary conditions are presented in Figure 8a. The objective was to verify whether the developed concrete model is able to predict with reasonable accuracy the experimental ultimate load reported by several authors with this type of test, see Table 3. Here $f_c$ is the concrete compressive strength, $E_f$ is the FRP elastic modulus, $b_c$ and $b_f$ are respectively the concrete and FRP width, and $l_b$ is the bond length. The numerical concrete samples were generated with the same material and geometry characteristics used in Section 2.5.1, therefore the concrete compressive strength was constant and equal to the value obtained from the compression tests in Section 2.5.1 (about 33 MPa). The FRP was modeled with truss elements perfectly bonded to the upper side of the concrete specimen (no separate adhesive layer was modeled). The elastic properties, cross-sectional area and length of the FRP matched those of the reference test results.

Table 3 shows that the agreement between numerical and experimental ultimate load is quite close for the first three considered specimens, where the concrete strength is similar to that of the numerical concrete. Not surprisingly, the last two specimens, which are characterized by a significantly larger concrete strength than in the numerical concrete, have a higher failure load than predicted by the model.

The damage variable distribution within the concrete sample at failure is shown in Figure 8b. The damaged area is generally localized in a thin layer of material underneath the FRP sheet, however in the portion of the bond length closest to the free end the fracture path becomes deeper and involves the underlying aggregates. The fracture path is obviously influenced by the location of the aggregates close to the surface, as will be shown in further tests in the following sections. Moreover, the comparison is approximate due to the 2D setting of the proposed model, as opposed to the 3D nature of the experimental results where non-negligible width effects are often registered (see also Section 4.3). Nevertheless, the overall results of these benchmark simulations confirm that the mesomechanical concrete model does provide reasonable predictions not only for the pure tensile and compressive behavior but also for FRP-concrete bond tests.

## 3. MULTISCALE FORMULATION

In the following, a numerical homogenization framework is set up for the FRP-concrete interface to relate damage and failure processes taking place at the mesoscale to a macroscopic CZM. This framework substantially follows the approach proposed by Matouš et al. (2008) and reformulated by Cid Alfaro et al. (2010) and Verhoosel et al. (2010). The macro- and mesoscales are linked using a transition procedure based upon Hill's energy principle. The starting point of the approach is the definition of an RVE. In the present study, local periodicity of the interface is assumed. Moreover, the RVE considered in the following does not consider the influence of the primer and resin layers but only includes the superficial layer of concrete underneath the FRP sheet. In order for a detailed and realistic geometry to be described, experimental quantitative observations are needed and are possible extensions of the present work.

Note that the existence itself of an RVE for materials exhibiting softening behavior (and thus localization) has been questioned by several authors, see e.g. Gitman et al. (2007a,b) and Nguyen et al. (2010). However, the multiscale approach adopted in the present work is not a bulk homogenization scheme leading to a homogenized stress-strain relationship, but rather a cohesive interface homogenization scheme, deriving macroscopic relationships between stresses and relative displacements across the interface. As a result, the objectivity of results with respect to the RVE dimensions is not compromised, see also Verhoosel et al. (2010).

Consider two macroscopic domains $\Omega_i^M \subset \mathbb{R}^2$, $i = \{1, 2\}$ with external boundaries $\Gamma_i^M$, see Figure 9. The external boundaries are subjected to displacements $\hat{\mathbf{u}}_i^M$ and tractions $\hat{\mathbf{t}}_i^M$ at $\Gamma_{ui}^M$ and $\Gamma_{ti}^M$, respectively, whereas the portion $\Gamma_{coh}^M$ represents the interface between the domains. Thus the total external boundaries are given by $\Gamma_i^M = \Gamma_{ti}^M \cup \Gamma_{ui}^M \cup \Gamma_{coh}^M$, with $\Gamma_{ti}^M \cap \Gamma_{ui}^M \cap \Gamma_{coh}^M = \varnothing$. The response in a material point of the cohesive interfacial boundary is connected to the lower-scale response of a heterogeneous, mesoscopic domain $\Omega^m \subset \mathbb{R}^2$ . This is represented by a thin concrete layer with explicit representation of the largest aggregates. For establishing a connection between formulations at the macro- and mesoscale levels, it is assumed that the mesoscopic domain can be considered as an RVE. Discussion on the dimensions of the RVE will follow in Section 4.1.

### *3.1. Governing equations at the macroscale*

The equilibrium condition for an arbitrary material point in the macroscopic domains $\Omega_i^M$ depicted in Figure 9 is

$$\operatorname{div}\left(\boldsymbol{\sigma}^M\right) = \mathbf{0} \qquad \text{in } \Omega_i^M \tag{15}$$

where $\boldsymbol{\sigma}^M$ represents the Cauchy stress tensor, and the body forces have been omitted. The boundary conditions for the macroscopic domains are given by

$$\boldsymbol{\sigma}^M \cdot \mathbf{n}_i^M = \hat{\mathbf{t}}_i^M \qquad \text{on } \Gamma_{ti}^M \tag{16}$$

$$\mathbf{u}^M = \hat{\mathbf{u}}_i^M \qquad \text{on } \Gamma_{ui}^M \tag{17}$$

where $\hat{\mathbf{t}}_i^M$ and $\hat{\mathbf{u}}_i^M$ are respectively the imposed tractions and the imposed displacements on the external boundaries $\Gamma_{ti}^M$ and $\Gamma_{ui}^M$ with outward unit normal $\mathbf{n}_i^M$. Across the cohesive boundary $\Gamma_{coh}^M$ ($\mathbf{n}_1^M = -\mathbf{n}_2^M = \mathbf{n}^M$) the tractions $\mathbf{t}^M$ are related to $\boldsymbol{\sigma}^M$ through the equilibrium condition

$$\boldsymbol{\sigma}^M \cdot \mathbf{n}^M = \mathbf{t}^M\left(\llbracket \mathbf{u}^M \rrbracket\right) \qquad \text{on } \Gamma_{coh}^M \tag{18}$$

where $\llbracket \mathbf{u}^M \rrbracket$ denotes the displacement discontinuity between the domains $\Omega_1^M$ and $\Omega_2^M$ across the cohesive interface. The macroscopic boundary value problem further includes the kinematic relations, which e.g. under the small-strain assumption read

$$\boldsymbol{\varepsilon}^M = \nabla^{sym}\mathbf{u}^M \tag{19}$$

with $\boldsymbol{\varepsilon}^M$ as the macroscopic strain tensor and $\nabla^{sym}$ as the symmetric part of the gradient operator, and the constitutive relations $\boldsymbol{\sigma}^M\left(\boldsymbol{\varepsilon}^M\right)$ in $\Omega_i^M$ and $\mathbf{t}^M\left(\llbracket \mathbf{u}^M \rrbracket\right)$ on $\Gamma_{coh}^M$. The aim of this paper is to derive the latter relations by means of the homogenization method discussed in Sections 3.3 and 3.4. Note that the framework proposed in this paper is independent of the considered macroscale formulation for discrete crack modelling. The two most commonly used approaches for modelling quasi-brittle failure are the use of interface elements (Camacho and Ortiz 1996) and, more recently, partition of unity-based methods (Wells and Sluys 2001, Moës and Belytschko 2002). Any of these approaches may be used in conjunction with the proposed homogenization method, provided a relationship such as $\mathbf{t}^M\left(\llbracket \mathbf{u}^M \rrbracket\right)$ is needed.

### *3.2. Governing equations at the mesoscale*

The two-dimensional domain $\Omega^m$ shown in Figure 10, i.e. a rectangular domain of width $w$ and thickness $t$, is studied on the mesoscale. Although the geometry of the mesoscale overall domain is regular, the material is highly heterogeneous. At this scale, displacements and displacement gradients are assumed to be small, thereby allowing for a linear kinematics description.

The equilibrium requirement for a material point within $\Omega^m$ can be expressed as

$$\operatorname{div}\left(\boldsymbol{\sigma}^m\right) = \mathbf{0} \qquad \text{in } \Omega^m \tag{20}$$

with the boundary conditions

$$\boldsymbol{\sigma}^m \cdot \mathbf{n}^m = \hat{\mathbf{t}}^m \qquad \text{on } \Gamma_t^m \tag{21}$$

$$\mathbf{u}^m = \hat{\mathbf{u}}^m \qquad \text{on } \Gamma_u^m \tag{22}$$

Here, $\boldsymbol{\sigma}^m$ is the mesoscale Cauchy stress tensor, and $\hat{\mathbf{t}}^m$ and $\hat{\mathbf{u}}^m$ are respectively the imposed tractions and the imposed displacements on the external boundaries $\Gamma_t^m$ and $\Gamma_u^m$ with outward unit normal $\mathbf{n}^m$. The total external boundary of the RVE is given by $\Gamma^m = \Gamma_u^m \cup \Gamma_t^m$. The macroscopic boundary value problem further includes the kinematic relations, which in this work follow the small-strain assumption and thus read

$$\boldsymbol{\varepsilon}^m = \nabla^{sym} \mathbf{u}^m \tag{23}$$

with $\boldsymbol{\varepsilon}^m$ as the mesoscale strain tensor, and the constitutive relations $\boldsymbol{\sigma}^m(\boldsymbol{\varepsilon}^m)$ in $\Omega^m$. In this contribution, the damage processes taking place at the mesoscale are described using a local damage model (Section 2.3). However, alternative formulations such as interface elements or partition of unity methods could be used equally well also at the mesoscale.

The principle of virtual work at the mesoscale leads to

$$\int_{\Omega^m} \boldsymbol{\sigma}^m : \boldsymbol{\delta\varepsilon}^m d\Omega^m = \int_{\Gamma_t^m} \hat{\mathbf{t}}^m \cdot \boldsymbol{\delta}\mathbf{u}^m d\Gamma_t^m \tag{24}$$

which must be satisfied for any admissible variational mesoscale displacement $\boldsymbol{\delta}\mathbf{u}^m$ satisfying $\boldsymbol{\delta}\mathbf{u}^m = \mathbf{0}$ on $\Gamma_u^m$.

### *3.3. RVE boundary conditions*

In order to establish a connection between the responses of the macroscale and mesoscale domains shown in Figure 9, the mesoscale displacement field $\mathbf{u}^m$ is expressed in terms of the macroscale displacement field $\mathbf{u}^M$ and a fluctuating displacement field $\tilde{\mathbf{u}}$ as

$$\mathbf{u}^m\left(\mathbf{x}^M, \mathbf{x}^m\right) = \mathbf{u}^M\left(\mathbf{x}^M\right) + \tilde{\mathbf{u}}\left(\mathbf{x}^m\right) \tag{25}$$

where $\mathbf{x}^M$ and $\mathbf{x}^m$ respectively denote the locations of the macroscale and mesoscale material points at which $\mathbf{u}^M$ and $\tilde{\mathbf{u}}$ are evaluated. The fluctuating displacement field $\tilde{\mathbf{u}}$ accounts for the displacement variations generated by the mesostructural heterogeneities, as measured with respect to the (average) macroscopic displacement of the mesoscale RVE. The boundary conditions for the mesoscopic model are then given in terms of the mesoscopic fluctuation fields $\tilde{\mathbf{u}}$. The displacements of the four corner nodes 1-4 (Figures 9, 10) of the mesoscale RVE correspond to the (uniform) macroscopic deformation of a material point in the macroscopic cohesive interface $\Gamma_{coh}^M$, hence the displacement fluctuations there are equal to zero, i.e.

$$\tilde{\mathbf{u}}^n = \mathbf{0} \qquad \text{with } n \in \{1, 2, 3, 4\} \tag{26}$$

Moreover, due to the consideration of the sample as a periodic cell along the $x_1^m$ direction, periodic boundary conditions for the fluctuation field are applied to the left ($L$) and right ($R$) edges of the RVE, as follows

$$\tilde{\mathbf{u}}^L(s_2) \quad = \tilde{\mathbf{u}}^R(s_2) \qquad \hat{\mathbf{t}}^{m,L}(s_2) = -\hat{\mathbf{t}}^{m,R}(s_2) \tag{27}$$

whereas a zero fluctuation field is assumed on the top ($T$) and bottom ($B$) edges of the RVE, i.e.

$$\tilde{\mathbf{u}}^T(s_1) \quad = \quad \mathbf{0} \quad \tilde{\mathbf{u}}^B(s_1) = \mathbf{0} \tag{28}$$

In the above equations, $s_1$ is a local coordinate along the $\Gamma_T^m$ and $\Gamma_B^m$ boundaries of the RVE, and $s_2$ is a local coordinate along the $\Gamma_L^m$ and $\Gamma_R^m$ boundaries. As a result of Eq. (25), Eqs. (27) and (28) lead to

$$\mathbf{u}^{M,R} = \mathbf{u}^{M,L} + \mathbf{u}^2 - \mathbf{u}^1 \quad \mathbf{u}^{M,T} = \mathbf{u}^4 \quad \mathbf{u}^{M,B} = \mathbf{u}^1 \tag{29}$$

Consistently with the above assumptions, the RVE is here subjected to the boundary conditions depicted in Figure 10. Periodic boundary conditions are applied on the lateral sides, due to the assumed local periodicity. The lower edge is considered fixed, whereas the upper edge is subjected to a monotonically

increasing uniform displacement. Hence the macroscopic displacement jump across the macroscale cohesive interface can be related to the displacement difference of two opposite corner nodes at the top and bottom surfaces of the RVE as

$$[\![\mathbf{u}^M]\!] = \mathbf{u}^{M,T} - \mathbf{u}^{M,B} = \mathbf{u}^4 - \mathbf{u}^1 = \mathbf{u}^3 - \mathbf{u}^2 = \mathbf{u}^4 = \mathbf{u}^3 = \hat{\mathbf{u}}_\alpha^m \tag{30}$$

where $\hat{\mathbf{u}}_\alpha^m$ is the displacement applied to the top surface of the RVE along the desired angle $\alpha$ (Figure 10). Depending upon the direction of this applied displacement, pure mode-I, mode-II or mixed-mode conditions with a desired mode mixity (here intended as a "displacement-based" mode mixity) can be obtained.

### *3.4. Derivation of the macroscopic interfacial traction*

In order to establish an expression for the macroscopic traction, $\mathbf{t}^M$, in a material point at the macroscale cohesive interface $\Gamma_{coh}^M$, Hill's averaging principle is applied. This principle states that the spatial average of the virtual work at the mesoscale, $\overline{\delta W^m}$, needs to be equal to the virtual work in a local material point of the macroscale cohesive interface, $\delta W_{coh}^M$, i.e.,

$$\delta W_{coh}^M = \overline{\delta W^m} \tag{31}$$

where

$$\delta W_{coh}^M = \mathbf{t}^M \cdot \delta[\![\mathbf{u}^M]\!] = \mathbf{t}^M \cdot \delta\mathbf{u}^4 \tag{32}$$

due to Eq. (30), and

$$\overline{\delta W^m} = \frac{1}{w}\delta W^m = \frac{1}{w}\int_{\Omega^m} \boldsymbol{\sigma}^m : \boldsymbol{\delta\varepsilon}^m d\Omega^m \tag{33}$$

Note from the above expression that the averaging procedure is performed by dividing the total virtual work of the mesoscale RVE by its width $w$. The height of the RVE does not need to be taken into account, since the macroscale geometrical object is a cohesive surface $\Gamma_{coh}^M$ with zero thickness (Cid Alfaro et al. 2010). The detailed derivation, deferred to the Appendix, leads to the final expression

$$\mathbf{t}^M = \frac{1}{w}\int_{\Gamma_T^m} \hat{\mathbf{t}}^{m,T} d\Gamma_t^m \tag{34}$$

Obviously, within an FE discretization the integral term in the right-hand side of Eq. (34) is approximated by the summation of the nodal forces at the top edge of the RVE. Thus the macroscopic tractions in the two directions are obtained as the summation of the reaction forces in the same directions at all the nodes of the upper edge of the RVE.

## 4. NUMERICAL RESULTS

### *4.1. Identification of the RVE*

In the previous section, a mesomechanical problem has been defined on which computational homogenization is carried out. In order for results of the homogenization process to be valid, the sample must qualify as an RVE. First of all, in order for the underlying assumption of scale separation to hold, thickness and width of the RVE must be suitably larger than the maximum aggregate size. A further basis for the choice of the thickness is the experimental observation that the layer of concrete involved by the damage mechanisms during debonding tests of FRP-concrete joints typically features a thickness between 20 and 50 mm (see e.g. Ferracuti et al. 2007).

In order to determine an appropriate width of the sample, simulations have been performed for variable widths ranging from 50 to 100 mm, under both mode-I and mode-II conditions. In these analyses we considered a thickness of 30 mm. Results are illustrated in Figures 11 and 12. Each numerical test has been repeated three times, obtaining three different geometries due to the random generation of the mesostructure.

Figure 11 shows the macroscopic cohesive behavior obtained from the RVE under pure mode-I loading. Figures 11a,c,e refer to the specimens directly obtained by the geometry procedure illustrated earlier. As aggregates are automatically generated at a minimum distance from the boundary of the domain, a superficial

layer of mortar is produced. As a result, failure tends to be localized in this layer. If the superficial elements in the FE model are removed so that some aggregate particles are present in the outer layer (Figures 11b,d,f), the damage distribution involves a thicker material region and the mode-I strength and fracture energy of the interface are consequently increased. For this reason, all subsequent numerical results have been obtained by removing the superficial layer of elements. (Note that, in real applications, it is quite common to remove the superficial mortar layer and expose the underlying aggregates e.g. through sandblasting in order to increase the interface strength). In any case, the results of the homogenization procedure in terms of cohesive response, peak normal stress, and mode-I fracture energy (i.e., area underneath the mode-I cohesive response) appear reasonably stable with increasing specimen width. As expectable, larger widths tend to lead to less scatter in results from the three different realizations. Similar results are obtained under mode-II loading conditions, as shown in Figure 12. Upon this round of numerical tests, a width of 100 mm has been chosen as the RVE width and has been used in all subsequent simulations.

A further series of analyses was performed to verify the effect of the RVE thickness of results. Results are reported in Figures 13 and 14. Once again each numerical test has been repeated three times, obtaining three different geometries. The results in terms of cohesive response, peak normal stress, and mode-I and mode-II fracture energy first vary with increasing specimen thickness and then approximately stabilize. Note that the initial (elastic) stiffness of the mode-I response indefinitely decreases with increasing specimen thickness, as it is reasonable to expect. The thickness effect is more pronounced for the mode-I quantities than for the mode-II ones. From the reported results, a thickness of 40 mm seems to be the desirable value to attain nearly stable results under mode-I conditions, whereas a thickness of 30 mm is sufficient under mode-II conditions. For simplicity, all subsequent simulations have been conducted for a thickness of 30 mm.

### *4.2. Homogenized mixed-mode cohesive zone behavior*

The macroscopic mixed-mode CZ behavior obtained from the homogenization procedure is illustrated in Figure 15 for one of three tested numerical specimens. Both shear and normal interfacial stresses are plotted as functions of shear and normal relative displacements at the interface. The observed behavior displays several interesting features. The mode-II CZ response (shear stress vs. shear relative displacement for $\alpha = 0°$, Figure 15a) appears qualitatively similar to the phenomenological laws often adopted in the literature, see also the comparison in Section 4.3. It features a nearly linear ascending branch, followed by an abrupt but small decrease in shear stress after a first peak, a subsequent increase with a second peak, and a final descending branch. The mode-I CZ response (normal stress vs. normal relative displacement for $\alpha = 90°$, Figure 15d) displays an initial linear branch followed by a single distinct peak and a descending branch. The mixed-mode responses feature both normal and shear stresses and relative displacements, whereby shear (normal) stresses evolve similarly as in the pure mode-II (mode-I) response. For the lowest mixed-mode angles (15 to 45°) part of the response leads to negative (i.e. compressive) stresses after the positive descending branch.

Figure 16 displays the peak stresses of the CZ responses in shear and peel and the relative fracture energies as functions of angle $\alpha$. Note that the mode-II (mode-I) fracture energy is computed as the area subtended by the positive part of the shear (normal) CZ response curve. The mode-II fracture energy results significantly larger than the mode-I value, which agrees well with previous experimental as well as theoretical results (De Lorenzis and Zavarise 2008). Moreover, the value of the mode-II fracture energy is quantitatively in agreement with the values found or adopted in previous investigations, see e.g. Yao et al. (2005) and Chen et al. (2007). Figure 17 summarizes results in the form of failure envelopes, both in terms of stresses and of fracture energies. Both envelopes have convex shapes, as expected from theoretical considerations. The shape of the stress envelope is non-linear whereas that of the fracture energy envelope is nearly linear.

In Figures 18-19, normal and shear interfacial stresses are plotted as functions of the magnitude of the imposed displacement $\hat{\mathbf{u}}_\alpha^m$. A few states are marked on each curve and the corresponding distributions of the damage variable within the RVE are given in Figures 20 to 26. It is evident that lower mode-mixity angles $\alpha$ lead to a more diffuse distribution of damage within the RVE, which translates into a larger dissipated energy, whereas angles closer to 90° determine a simpler damage contour plot resembling a crack pattern approximately perpendicular to the applied load, such as in the pure tensile test of Section 2.5. These observations suggest that larger fracture energies can be obtained through more complex damage patterns which in turn are induced by the heterogenous nature of the material as well as from the loading conditions. One of the natural extensions of the proposed approach would thus be the possibility to tailor and optimize the lower-scale features to achieve a desired macroscale response.

*4.3. Comparison with available mode-II CZ models*

As follows, the mode-II CZ laws obtained through the proposed homogenization procedure are compared with three phenomenological analytical models taken from the available literature on FRP-concrete bond. These models (often referred to as "bond-slip models") and their parameters are summarized in Table 4. Here $\tau$ is the shear stress and $s$ the tangential relative displacement, $\tau_{max}$ is the mode-II cohesive strength, $f_t$ is the concrete tensile strength, $G_f$ is the mode-II fracture energy, and $s_0$, $\beta_w$, $\alpha$ and $\alpha_1$ are additional parameters. In Figure 27, the mode-II CZ laws obtained through the proposed homogenization procedure are plotted along with the analytical curves. Note that the analytical models are applied considering as material properties for concrete those obtained from the compressive and tensile tests in Section 2.5.1. Considering that the numerical and analytical curves stem from completely different approaches, the agreement can be considered reasonably good. The model by Lu et al. (2005) is applied both with $\beta_w$ (width correction factor) as given by Table 4, and with $\beta_w = 1$. In the latter case, its cohesive strength predictions are quite close to those of the homogenized model. Note that the comparison is approximate due to the 2D nature of the proposed model, as opposed to the 3D experimental results used for calibration of the analytical models. This justifies the presence of the width effects in the analytical formulae, which cannot be accounted for in the present numerical context.

## 5. CONCLUSIONS

This paper proposes a multiscale approach through which CZ laws for FRP-concrete interfaces or other interfaces in concrete under variable mode mixity can be derived through a detailed examination of the mesoscale geometry and a suitable constitutive modeling of the constituent materials. A necessary intermediate step for the proposed formulation has been the setup of a mesoscale concrete model. The results show the capability and flexibility of the approach to translate the features of the mesoscale geometry into macroscopic results, in terms of concrete tensile and compressive response, as well as of mixed-mode CZ laws for the FRP-concrete interface under the assumption that failure is controlled by the properties of the superficial concrete layer. Possible further extensions include the improvement of the material model (e.g. by adopting a mesh-insensitive constitutive description for the matrix as well as the ITZ), and the analysis of the role of the aggregate shape, size and distribution on the macroscopic results. Moreover, a detailed examination of the mesostructure of the interfacial layer for FRP bonded to concrete reveals a more complex nature than assumed herein, including layers of primer, resin, and the presence of resin-filled pores in the concrete intersecting the crack path (De Lorenzis et al. 2001). Hence, the extension of the present work to more realistic mesoscale geometries and to the 3D setting would be of significance. Finally, being able to shed light on the role played by the mesoscale parameters on key quantitative aspects of the macroscopic response such as the fracture energy under a given mode mixity, the proposed approach may allow for tailoring and optimization of the lower-scale features to achieve a desired macroscale response.

## 6. ACKNOWLEDGEMENTS

This research was funded by the European Research Council, ERC Starting Researcher Grant "INTERFACES", Grant Agreement N. 279439.

## 7. REFERENCES

[1] Bažant Z.P., Oh B.H. (1983). Crack band theory for fracture of concrete. Materials and Structures, 16(93): 155-177.

[2] Bažant Z.P., Tabbara M.R., Kazemi M.T., Pijaudier-Cabot G. (1990). Random particle model for fracture of aggregate or fiber composites. Journal of Engineering Mechanics, ASCE, 116(8): 1686–1705.

[3] Caballero A., Lopez C.M., Carol I. (2006). 3D meso-structural analysis of concrete specimens under uniaxial tension. Computer Methods in Applied Mechanics and Engineering, 195: 7182-7195.

[4] Camacho G.T., Ortiz M. (1996). Computational modelling of impact damage in brittle materials. International Journal of Solids and Structures, 33(20–22): 2899–2938.

[5] Chai H. (2003). Interfacial mixed-mode fracture of adhesive bonds undergoing large deformation. International Journal of Solids and Structures, 40: 6023–6042.

[6] Chen J.F., Teng J.G. (2001). Anchorage strength models for FRP and steel plates bonded to concrete. Journal of Structural Engineering, ASCE 127(7): 784–791.

[7] Chen J.F., Yuan H., Teng J.G. (2007). Debonding failure along a softening FRP-to-concrete interface between two adjacent cracks in concrete members. Engineering Structures, 29: 259–270.

[8] Cid Alfaro M.V., Suiker A.S.J., Verhoosel C.V., de Borst R. (2010). Numerical homogenization of cracking processes in thin fibre-epoxy layers. European Journal of Mechanics A/Solids, 29: 119–131.

[9] De Lorenzis L., Miller B., Nanni A. (2001) Bond of FRP laminates to concrete. ACI Materials Journal, 98(3): 256–264.

[10] De Lorenzis L., Zavarise G. (2008). Modeling of mixed-mode debonding in the peel test applied to superficial reinforcements. International Journal of Solids and Structures, 45: 5419–5436.

[11] De Lorenzis L. (2012), Some recent results and open issues on interface modeling in civil engineering structures, Materials and Structures, 45(4): 477-503.

[12] De Lorenzis, L., Zavarise, G. (2009), Cohesive zone modeling of interfacial stresses in plated beams, International Journal of Solids and Structures, 46(24): 4181-4191.

[13] De Lorenzis L., Fernando D., Teng J.G. (2013), Coupled mixed-mode cohesive zone modeling of interfacial debonding in plated beams, International Journal of Solids and Structures, 50: 2477-2494.

[14] De Schutter G., Taerwe L. (1993). Random particle model for concrete based on Delaunay triangulation. Materials and Structures, 26(156): 67-73.

[15] Ferracuti B., Savoia M., Mazzotti C. (2007). Interface law for FRP-concrete delamination. Composite Structures, 80(4): 523–531.

[16] Geubelle P.H., Baylor, J. (1998). Impact-induced delamination of composites: a 2D simulation. Composites Part B: Engineering, 29B: 589-602.

[17] Gitman I.M., Askes H., Aifantis E.C. (2007a). Gradient elasticity with internal length and internal inertia based on the homogenisation of a Representative Volume Element. Journal of the Mechanical Behaviour of Materials, 18: 1-16.

[18] Gitman I.M., Askes H., Sluys L.J. (2007b). Representative volume: existence and size determination. Engineering Fracture Mechanics, 74 (16): 2518–2534.

[19] Häfner S., Eckardt S., Luther T., Könke, C. (2006). Mesoscale modeling of concrete: Geometry and numerics. Computers and Structures, 84: 450–461.

[20] Hirschberger C.B., Ricker S., Steinmann P., Sukumar N. (2009). Computational multiscale modelling of heterogeneous material layers. Engineering Fracture Mechanics, 76: 793–812.

[21] Hoefnagels J.P.M., Neggers J., Timmermans P.H.M., van der Sluis O., Geers M.G.D. (2010) Copper–rubber interface delamination in stretchable electronics. Scripta Materialia, 63: 875–878.

[22] Kafkalidis M.S., Thouless M.D. (2002). The effects of geometry and material properties on the fracture of single lap-shear joints. International Journal of Solids and Structures, 39: 4367–4383.

[23] Karbhari V.M., Engineer M., Eckel II D.A. (1997). On the durability of composite rehabilitation schemes for concrete: use of a peel test. Journal of Materials Science, 32: 147–156.

[24] Kouznetsova V., Brekelmans W.A.M., Baaijens F.P.T. (2001). An approach to micromacro modeling of heterogeneous materials. Computational Mechanics, 27: 37–48.

[25] Kulkarni M.G., Geubelle P.H., Matouš K. (2009). Multi-scale modelling of heterogeneous adhesives: effect of particle decohesion. Mechanics of Materials, 41: 573–583.

[26] Kulkarni M.G., Matouš K., Geubelle P.H. (2010). Coupled multi-scale cohesive modeling in heterogeneous adhesives. International Journal for Numerical Methods in Engineering, 84: 916-946.

[27] Li S., Thouless M.D., Waas A.M., Schroeder J.A., Zavattieri P.D. (2006). Mixed-mode cohesive-zone models for fracture of an adhesively bonded polymer matrix composite. Engineering Fracture Mechanics, 73: 64–78.

[28] Lopez C.M., Carol I., Aguado A. (2008). Meso-structural study of concrete fracture using interface elements. I: numerical model and tensile behavior. Materials and Structures, 41: 583-599.

[29] Lu X.Z., Teng J.G., Ye L.P., Jiang J.J. (2005). Bond-slip models for FRP sheets/plates bonded to concrete. Engineering Structures, 27: 920-937.

[30] Matouš K., Kulkarni M.G., Geubelle P.H. (2008). Multiscale cohesive failure modeling of heterogeneous adhesives. Journal of the Mechanics and Physics of Solids, 56: 1511–1533.

[31] Miehe C., Koch A. (2002). Computational micro-to-macro transitions of discretized microstructures undergoing small strains. Archive of Applied Mechanics, 72: 300–317.

[32] Moës N., Belytschko T. (2002). Extended finite element method for cohesive crack growth. Engineering Fracture Mechanics, 69(7): 813–833.

[33] Nakaba K., Toshiyuki K., Tomoki F., Hiroyuki Y. (2001). Bond behavior between fiber-reinforced polymer laminates and concrete. ACI Structural Journal, 98(3): 359-367.

[34] Nguyen V.P., Valls O.L., Stroeven M., Sluys L.J. (2010). On the existence of representative volumes for softening quasi-brittle materials – A failure zone averaging scheme. Computer Methods in Applied Mechanics and Engineering, 199: 3028-3038.

[35] Pan J., Leung C.K.Y. (2007). Debonding along the FRP–concrete interface under combined pulling/peeling effects. Engineering Fracture Mechanics, 74: 132–150.

[36] Pantano A., Averill R.C. (2004). A mesh-independent interface technology for simulation of mixed-mode delamination growth. International Journal of Solids and Structures, 41(14): 3809-3831.

[37] Pelissou C., Baccou J., Monerie Y., Perales F. (2009). Determination of the size of the representative volume element for random quasi-brittle composites. International Journal of Solids and Structures, 46: 2842–2855.

[38] Pijaudier-Cabot G., Mazars J. (2001). Damage models for concrete, in: Handbook of materials behavior models, J. Lemaitre (ed.) Chapter 6 - Damage models, Academic Press, New York, 500-513.

[39] Roy Y.A., Narasimhan R., Arora P.R. (1999). An experimental investigation of constraint effects on mixed mode fracture initiation in a ductile aluminium alloy. Acta Materialia, 47(5): 1587–1596.

[40] Savoia M., Ferracuti B., Mazzotti D. (2003). Non-linear bond-slip law for FRP-concrete interface. In: Proc. of 6th International Symposium on FRP reinforcement for concrete structures. Singapore: World Scientific Publications, 163-172.

[41] Schlangen E., van Mier J.G.M. (1992). Simple lattice model for numerical simulation of fracture of concrete materials and structures. Materials and Structures, 25(153): 534-542.

[42] Schorn H., Rode U. (1991). Numerical simulation of crack propagation from microcracking to fracture. Cement and Concrete Composites, 13(2): 87-94.

[43] Snozzi L., Caballero A., Molinari J.F. (2011). Influence of the meso-structure in dynamic fracture simulation of concrete under tensile loading. Cement and Concrete Research, 41(11): 1130-1142.

[44] Takeo K., Matsushita H., Makizumi T., Nagashima G. (1997). Bond characteristics of CFRP sheets in the CFRP bonding technique. In: Proc. of Japan concrete institute, vol. 19, no. 2. June, 1997. p. 1599–1604.

[45] Tan Z. (2002). Experimental research for RC beam strengthened with GFRP. Master thesis, Tsinghua University.

[46] Teng J.G., Zhu W.C., Tang C.A. (2004). Mesomechanical model for concrete - Part II: Applications. Magazine of Concrete Research, 56(6): 331–345.

[47] Tvergaard V., Hutchinson J.W. (1992). The relation between crack growth resistance and fracture process parameters in elastic-plastic solids, Journal of the Mechanics and Physics of Solids, 40(6): 1377-1397.

[48] Ueda T., Sato Y., Asano Y. (1999). Experimental study on bond strength of continuous carbon fiber sheet. In: Proceedings of 4th int. sym. on fiber reinforced polymer reinforcement for reinforced concrete structure, 407–416.

[49] Verhoosel C.V., Remmers J.J.C., Gutierrez M.A., de Borst R. (2010). Computational homogenization for adhesive and cohesive failure in quasi-brittle solids. International Journal for Numerical Methods in Engineering, 83: 1155–1179.

[50] Wan B., Sutton M.A., Petrou M.F., Harries K.A., Li N. (2004). Investigation of bond between fiber reinforced polymer and concrete undergoing global mixed mode I/II loading. ASCE Journal of Engineering Mechanics, 130 (12), 1467–1475.

[51] Wang Z.M., Kwan A.K.H., Chan H.C. (1999). Mesoscopic study of concrete I: generation of random aggregate structure and finite element mesh. Computers and Structures, 70: 533-544.

[52] Wells G.N., Sluys L.J. (2001). A new method for modelling cohesive cracks using finite elements. International Journal for Numerical Methods in Engineering, 50(12): 2667–2682.

[53] Wittmann F.H., Roelfstra P.E., Sadouki H. (1984). Simulation and Analysis of Composite Structures. Materials Science and Engineering, 68: 239-48.

[54] Wriggers P., Moftah S.O. (2006). Mesoscale models for concrete: Homogenisation and damage behaviour. Finite Elements in Analysis and Design, 42: 623 - 636.

[55] Wu Z.S., Yuan H., Yoshizawa H., Kanakubo T. (2001). Experimental/analytical study on interfacial fracture energy and fracture propagation along FRP-concrete interface. ACI International SP, 201(8): 133–152.

[56] Xu, X.-P., Needleman, A. (1994). Numerical simulations of fast crack growth in brittle solids, Journal of the Mechanics and Physics of Solids, 42(9): 1397-1434.

[57] Yao J., Teng J.G., Chen J.F. (2005). Experimental study on FRP-to-concrete bonded joints. Composites: Part B, 36, 99–113.

[58] Yuan H., Teng J.G., Seracino R., Wu Z.S., Yao J. (2004). Full range behavior of FRP-to-concrete bonded joints: a closed-form analytical solution. Engineering Structures, 26(5): 553–564.

[59] Zhu W.C., Teng J.G., Tang C. A. (2004). Mesomechanical model for concrete. Part I: model development. Magazine of Concrete Research, 56: 313 - 330.

[60] Zohdi T.I., Wriggers P. (2001). Computational micro-macro material testing, Archives of Computational Methods in Engineering, 8(2): 131–228.

| Material | $E_0$ (GPa) | $\nu_0$ | $k_0$ | $A_t$ | $B_t$ | $A_c$ | $B_c$ |
|---|---|---|---|---|---|---|---|
| Aggregates | 70 | 0.2 | - | - | - | - | - |
| Matrix | 20 | 0.2 | $3.5 \cdot 10^{-4}$ | 1 | 2500 | 1 | 500 |
| ITZ | 20 | 0.2 | $2.5 \cdot 10^{-4}$ | 1 | 2500 | 1 | 500 |

Table 1: Material parameters.

| $R_{agg}$ | $s$ | $D_{min}$ (mm) | $D_{max}$ (mm) | $\lambda_{min}$ | $\lambda_{max}$ | $\delta$ | $\gamma_{min}$ | $\gamma_{max}$ |
|---|---|---|---|---|---|---|---|---|
| $0.2, 0.3, 0.4$ | 3 | 4 | 10 | 1 | 3 | 0.7 | 0.05 | 0.15 |

Table 2: Geometry parameters.

| Specimen | FRP | | | Concrete | | Ultimate load (kN) | |
|---|---|---|---|---|---|---|---|
| | $b_f$ (mm) | $l_b$ (mm) | $E_f$ (GPa) | $f_c$ (MPa) | $b_c$ (mm) | Experimental | Numerical |
| Yuan et al. (2004) | 25 | 190 | 265 | 29.74 | 150 | 5.7 | 6.1 |
| Takeo et al. (1997) | 40 | 200 | 230 | 33.75 | 100 | 8.5 | 10.4 |
| Tan (2002) | 50 | 130 | 235 | 37.6 | 100 | 9.2 | 12.0 |
| Wu et al. (2001) | 40 | 250 | 390 | 72.0 | 100 | 23.5 | 11.0 |
| Ueda et al. (1999) | 100 | 200 | 230 | 57.4 | 500 | 38.0 | 33.4 |

Table 3: Comparison between experimental and numerical failure loads.

| Reference | Ascending branch $s \leq s_0$ | Descending branch $s > s_0$ | $\tau_{max}$ | $s_0$ | $\beta_w$ | $G_f$ | |
|---|---|---|---|---|---|---|---|
| Nakaba et al. (2001) | $\tau(s) = \tau_{max}\left(\frac{s}{s_0}\right)\left[3/\left(2+\left(\frac{s}{s_0}\right)^3\right)\right]$ | | $3.5 f_c^{0.19}$ | 0.065 | | | |
| Savoia et al. (2003) | $\tau(s) = \tau_{max}\left(\frac{s}{s_0}\right)\left[2.86/\left(1.86+\left(\frac{s}{s_0}\right)^{2.86}\right)\right]$ | | $3.5 f_c^{0.19}$ | 0.051 | | | |
| Lu et al. (2005) | $\tau(s) = \tau_{max}\sqrt{\frac{s}{As_0}}$ | $\tau(s) = \tau_{max} exp\left[-\alpha(s/s_0 - 1)\right]$ | $\alpha_1 \beta_w f_t$ | $0.0195 \beta_w f_t$ | $\sqrt{\frac{2.25 - b_f/b_c}{1.25 + b_f/b_c}}$ | $0.308 \beta_w^2 \sqrt{f_t}$ | |

Table 4: Analytical mode-II CZ models for the FRP-concrete interface.

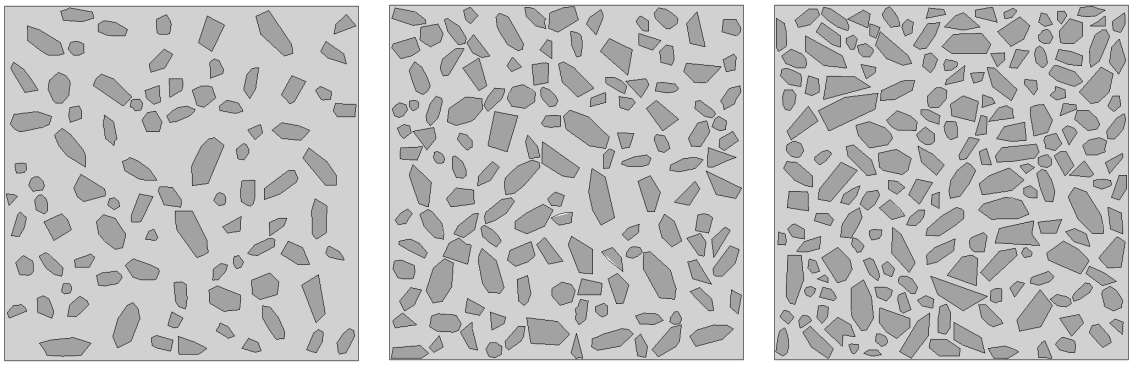

(a) (b) (c)

Figure 1: Numerical concrete specimen with different aggregate ratios: $R_{agg} = 0.2$ (a), 0.3 (b), 0.4 (c).

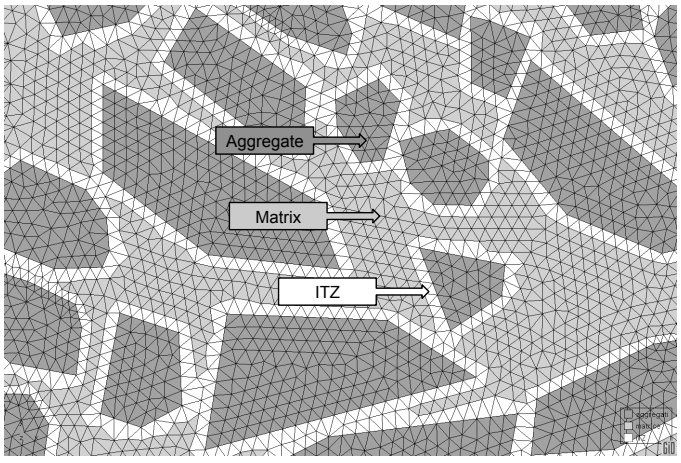


Figure 2: Meshing of the mesomechanical geometry with indication of the different phases.

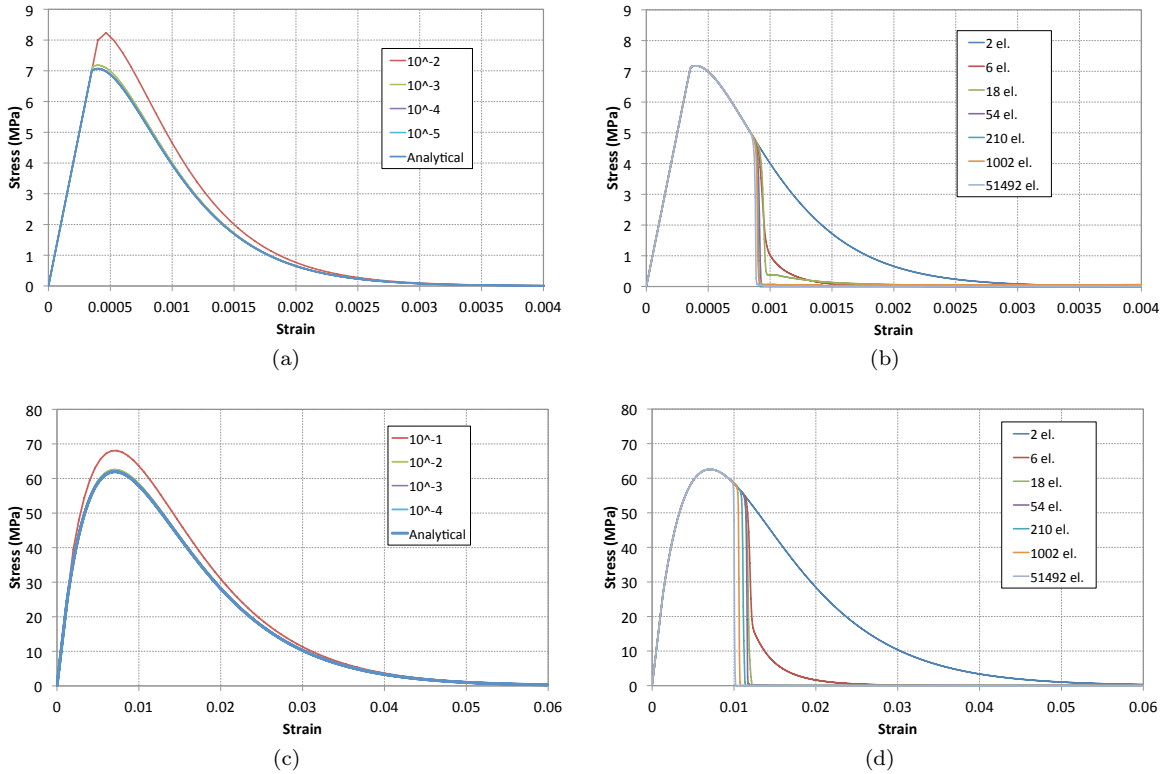


Figure 3: Analytical and numerical stress-strain curves of the matrix in uniaxial tension (a,b) and compression (c,d) for the model parameters in Table 1. Figures (a,c) illustrate calibration of the pseudo time-step for a mesh with 2 elements and Figures (b,d) demonstrate the mesh sensitivity effect resulting from the local damage modeling approach ($\Delta t = 10^{-3}$ in tension, $\Delta t = 10^{-2}$ in compression).

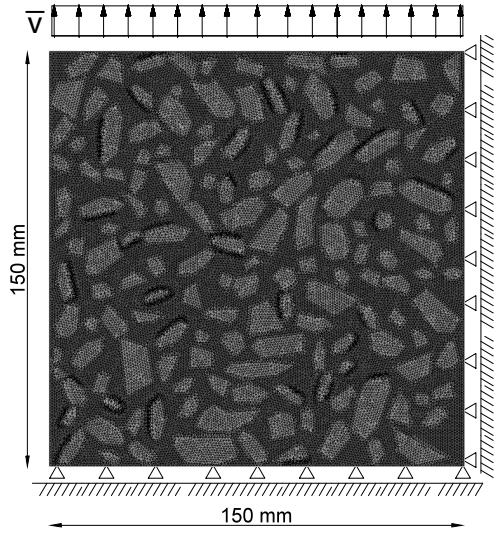


Figure 4: Geometry of a numerical concrete specimen subjected to tensile testing.

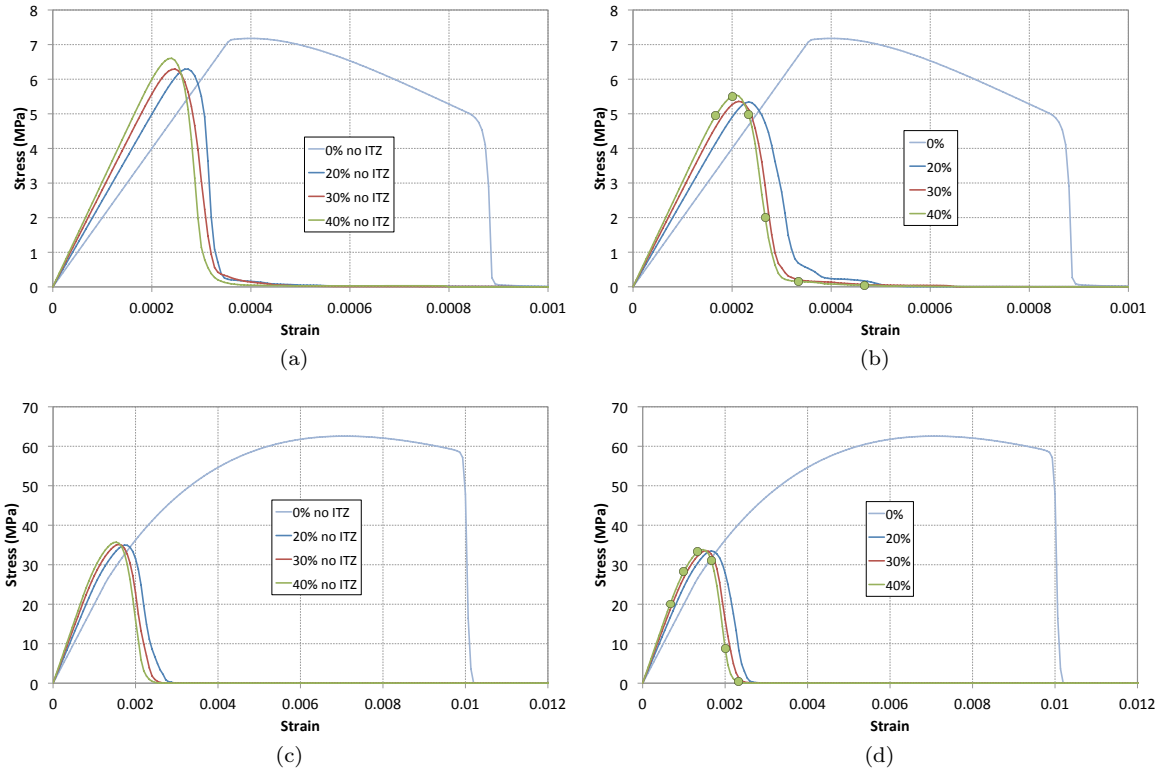


Figure 5: Analytical and numerical stress-strain curves of the concrete specimen in uniaxial tension (a,b) and compression (c,d) for the model parameters in Tables 2 and 1 with varying aggregate ratio $R_{agg}$. Figures (a,c) are obtained with no consideration of the ITZ, whereas Figures (b,d) consider an ITZ consisting in one layer of elements around each aggregate.

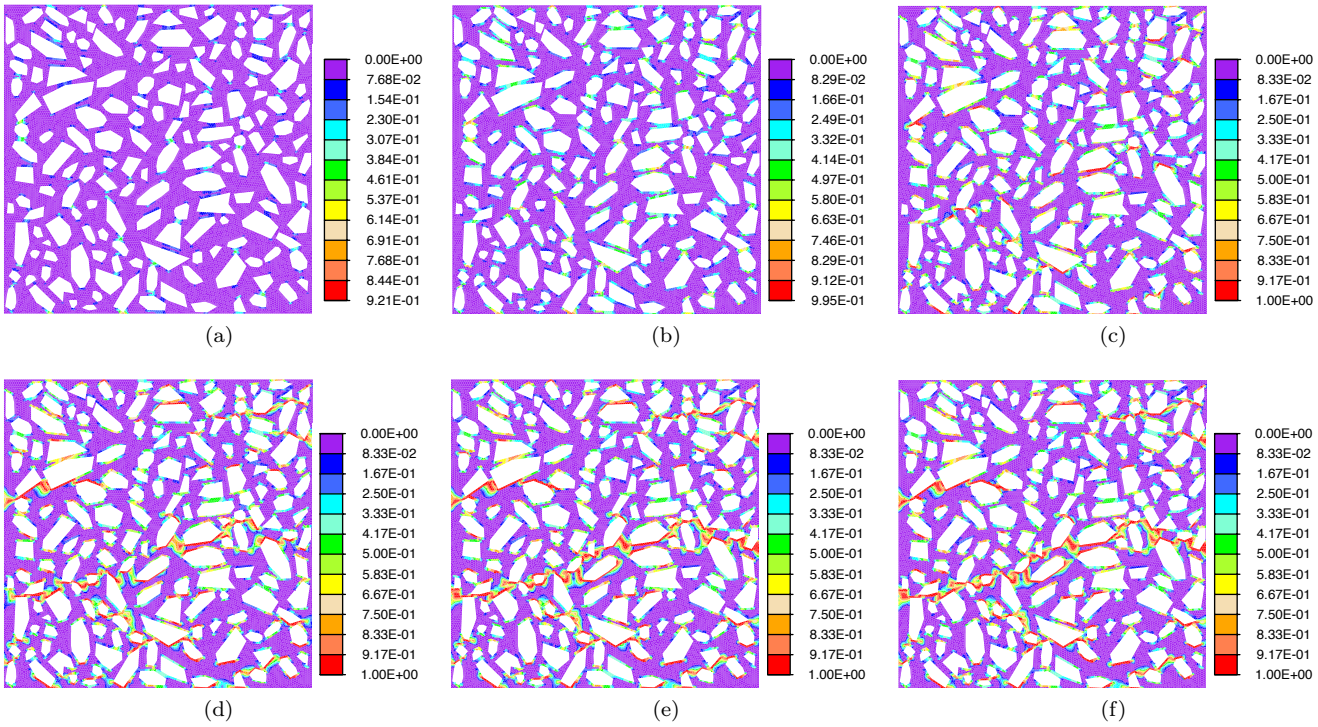


Figure 6: Damage variable distribution within the concrete sample ($R_{agg} = 40\%$ with ITZ) under uniaxial tension at the stages of loading indicated with the markers in Figure 5b.

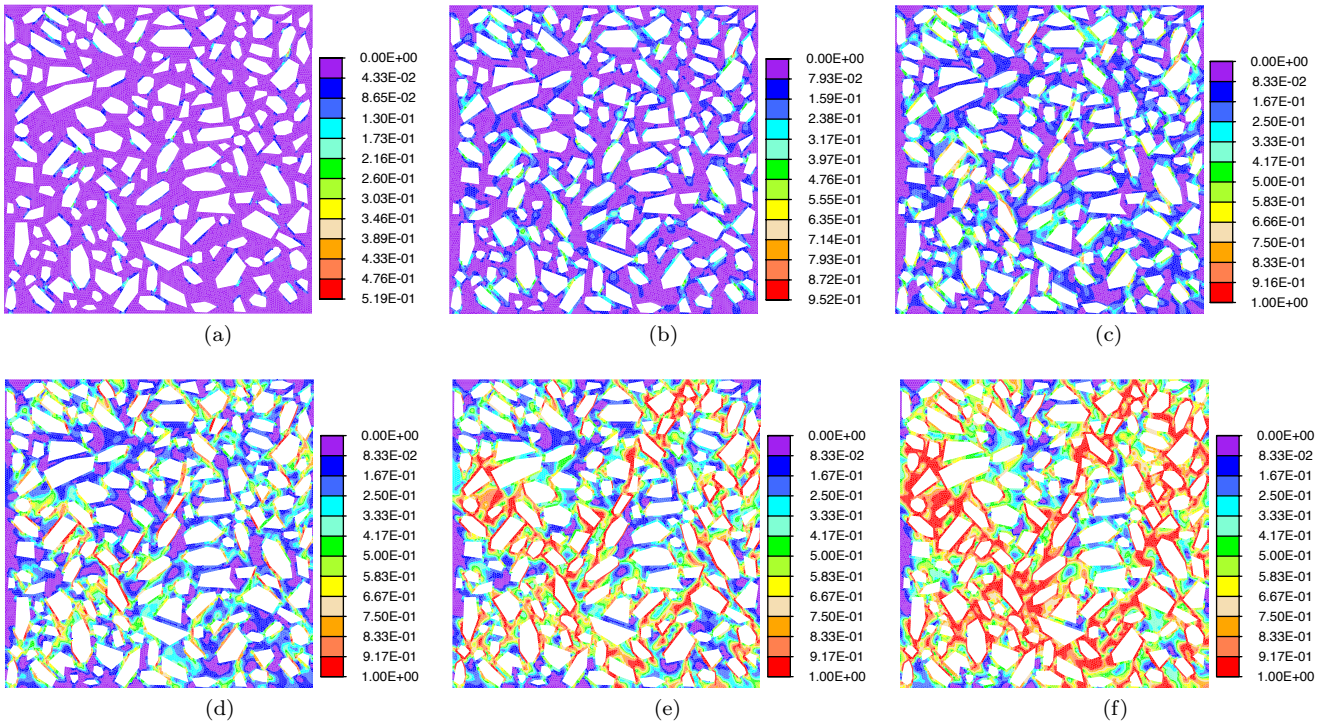


Figure 7: Damage variable distribution within the concrete sample ($R_{agg} = 40\%$ with ITZ) under uniaxial compression at the stages of loading indicated with the markers in Figure 5d.

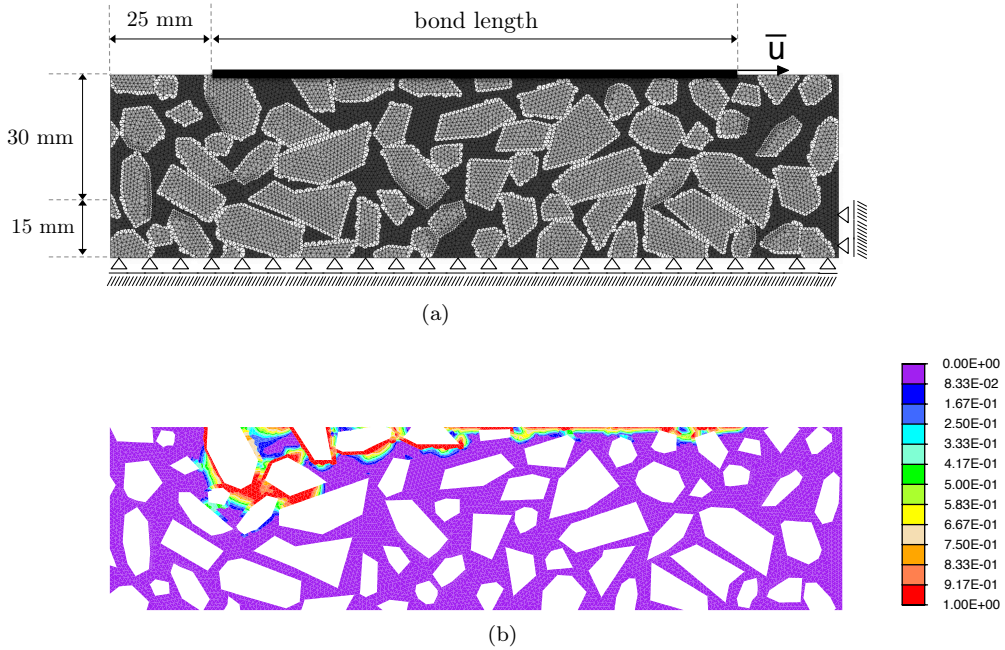


Figure 8: Pull–push shear test: geometry of a numerical concrete specimen (a) and damage variable distribution within the concrete sample at failure (b).

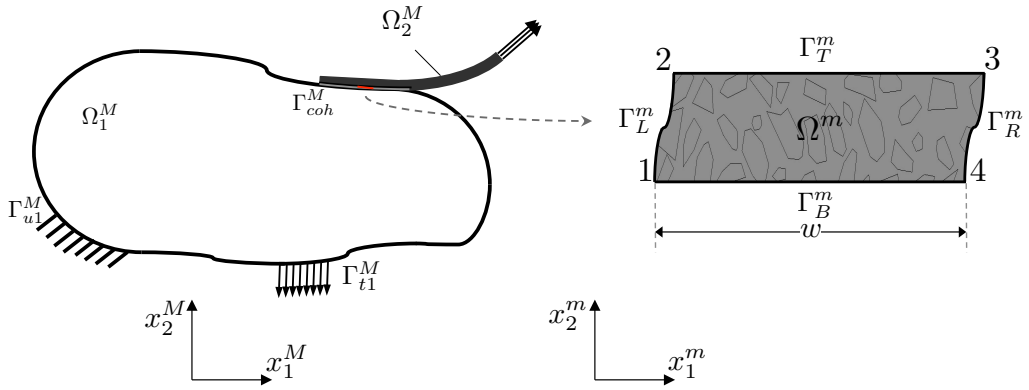


Figure 9: Generic representation of the macroscale (on the left) and of the mesoscale (on the right) models with the relevant symbols. The boundary $\Gamma_{coh}^M$ represents a cohesive interface.

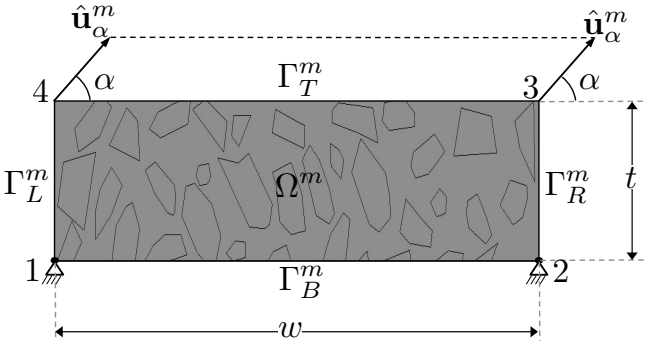


Figure 10: The RVE and its boundary conditions.

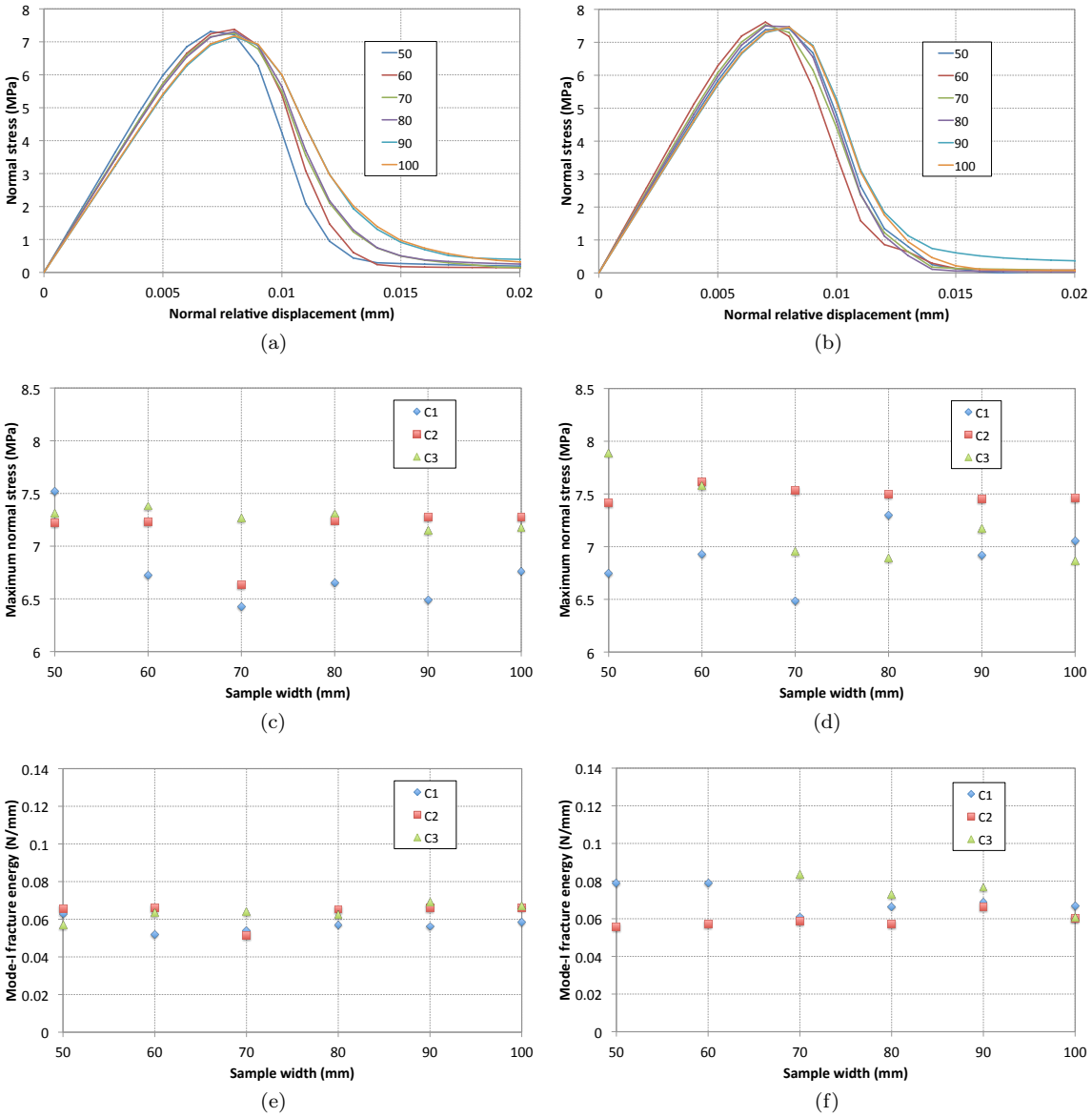


Figure 11: Effect of sample width on the mode-I cohesive behavior for samples with (a,c,e) and without (b,d,f) superficial matrix layer. Normal stress - relative displacement relationship for one representative specimen (a,b). Cohesive strength (c,d) and Mode-I fracture energy (e,f) as functions of the sample width for the three tested specimens.

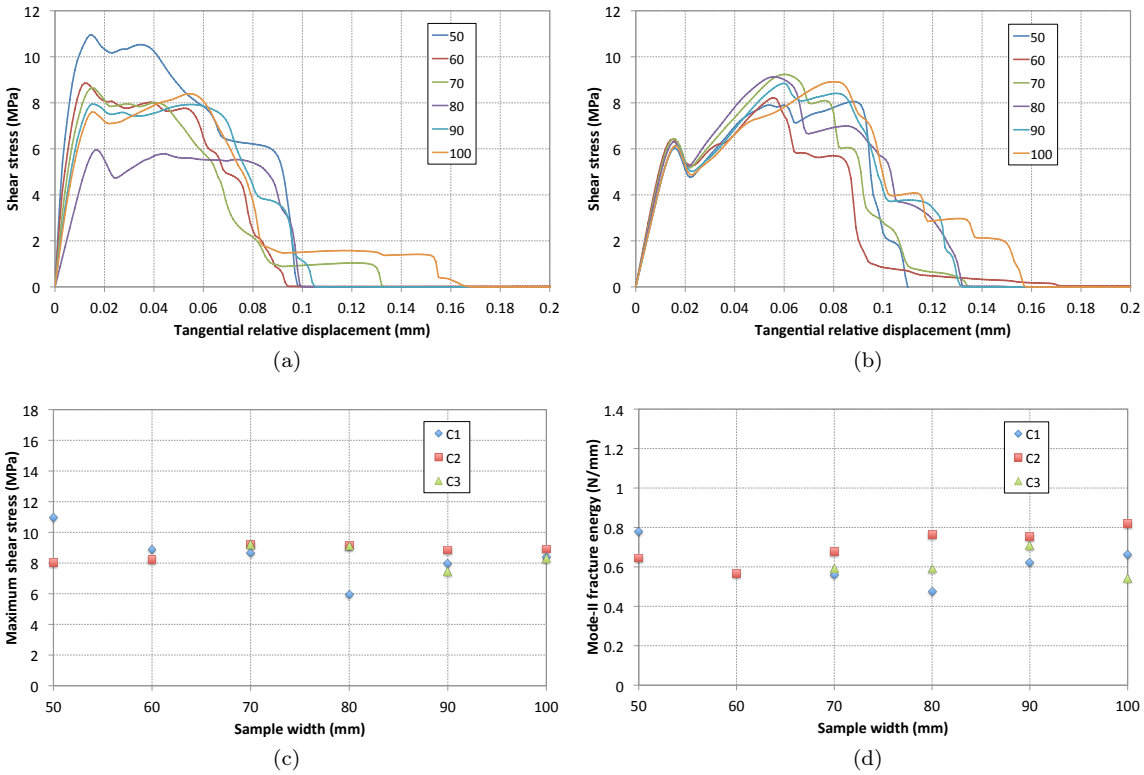


Figure 12: Effect of sample width on the mode-II cohesive behavior. Tangential stress - relative displacement relationships for two specimens (a,b). Cohesive strength (c) and Mode-II fracture energy (d) as functions of the sample width for the three tested specimens.

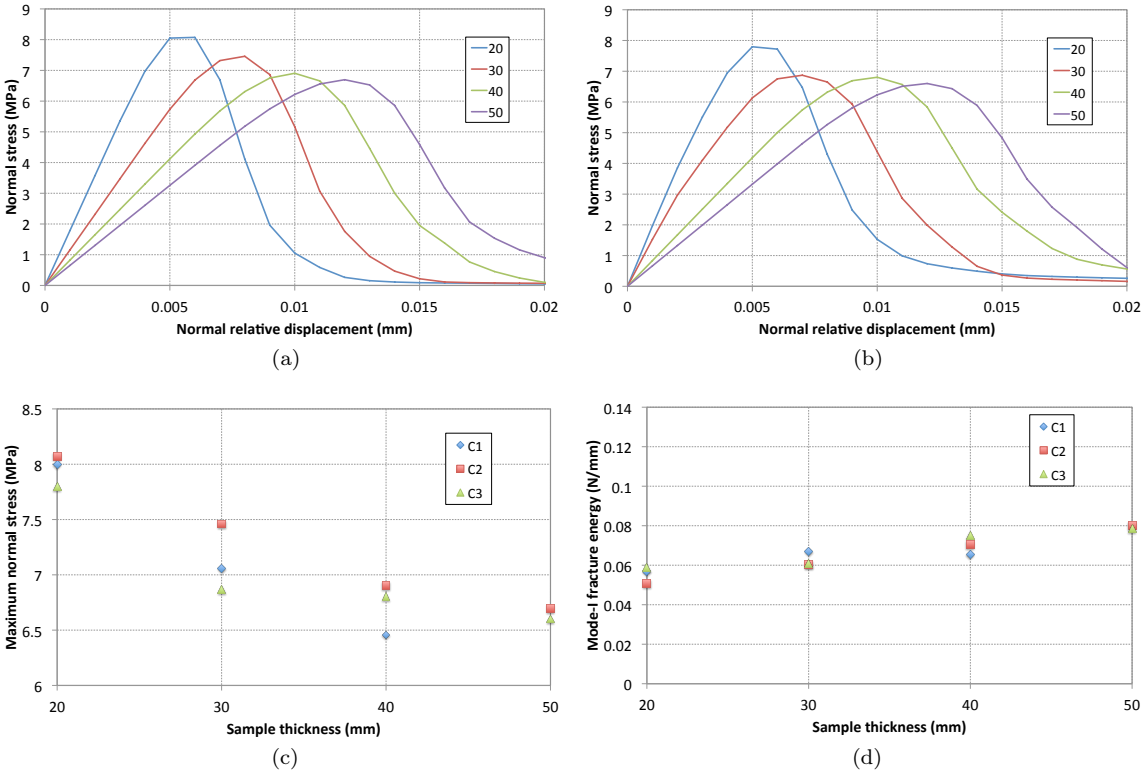


Figure 13: Effect of sample thickness on the mode-I cohesive behavior. Normal stress - relative displacement relationships for two specimens (a,b). Cohesive strength (c) and Mode-I fracture energy (d) as functions of the sample thickness for the three tested specimens.

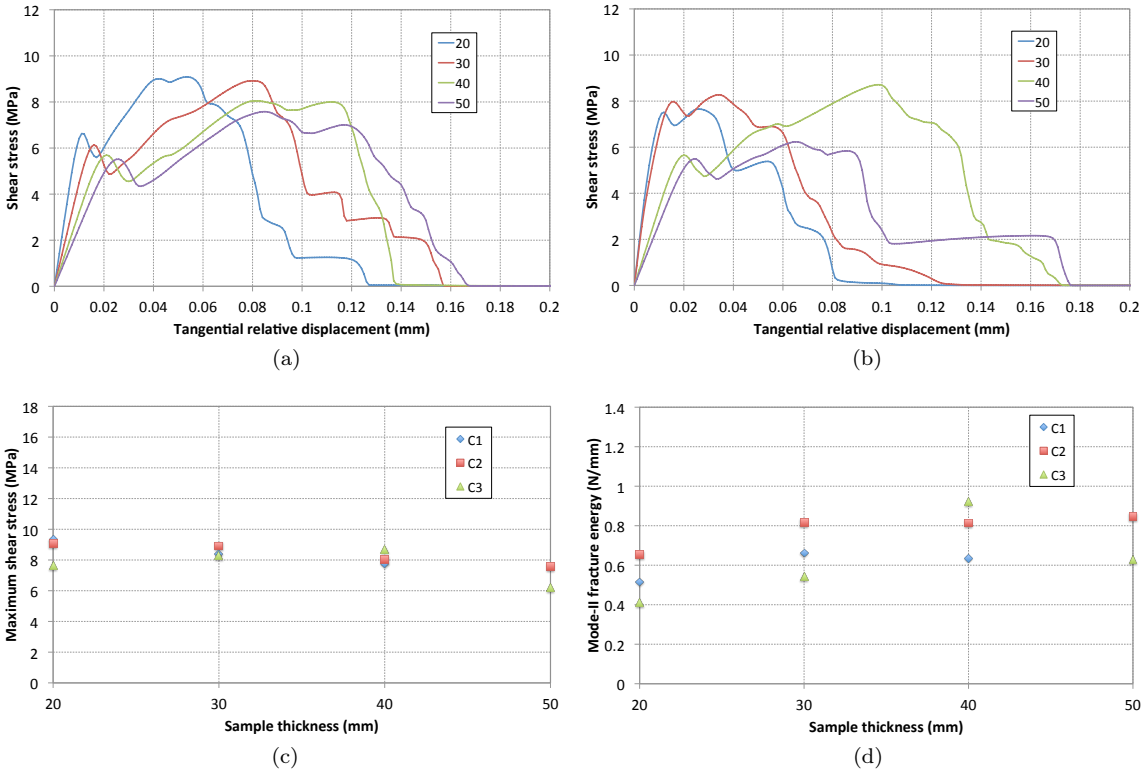


Figure 14: Effect of sample thickness on the mode-II cohesive behavior. Tangential stress - relative displacement relationships for two specimens (a,b). Cohesive strength (c) and Mode-II fracture energy (d) as functions of the sample thickness for the three tested specimens.

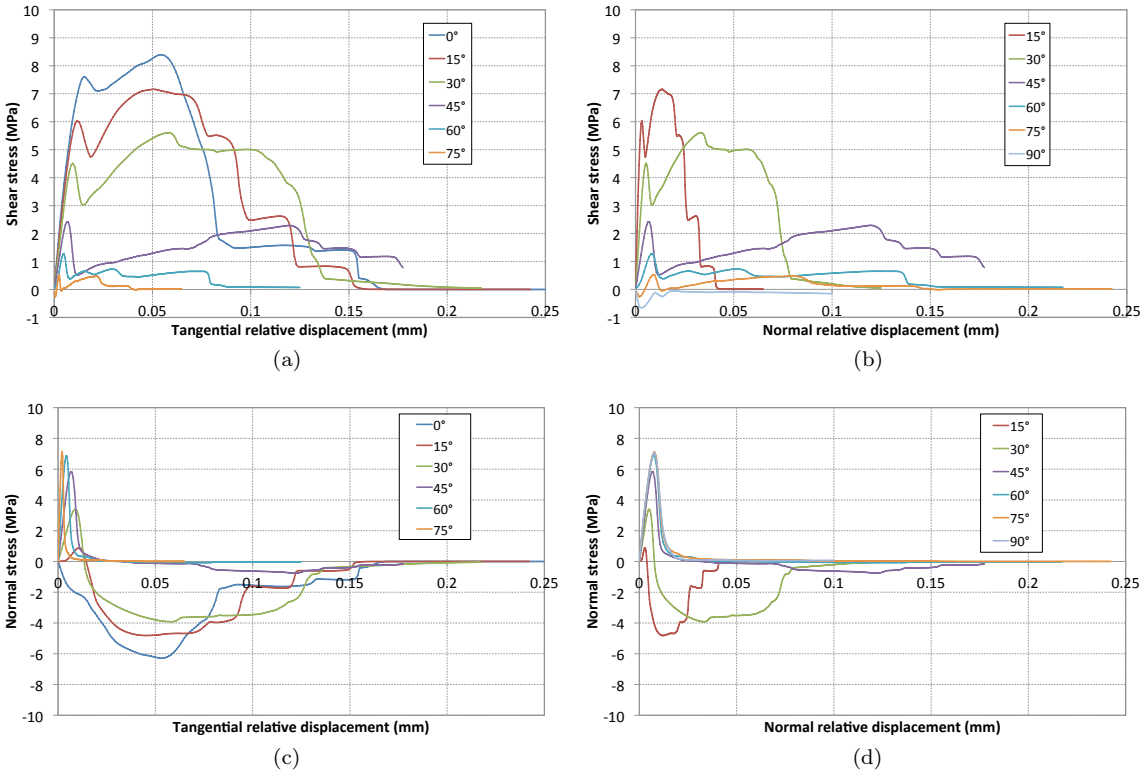


Figure 15: Mixed-mode cohesive behavior. Tangential stress vs. tangential (a) and normal (b) relative displacement relationships, and normal stress vs. tangential (c) and normal (d) relative displacement relationships for one of the numerical tests.

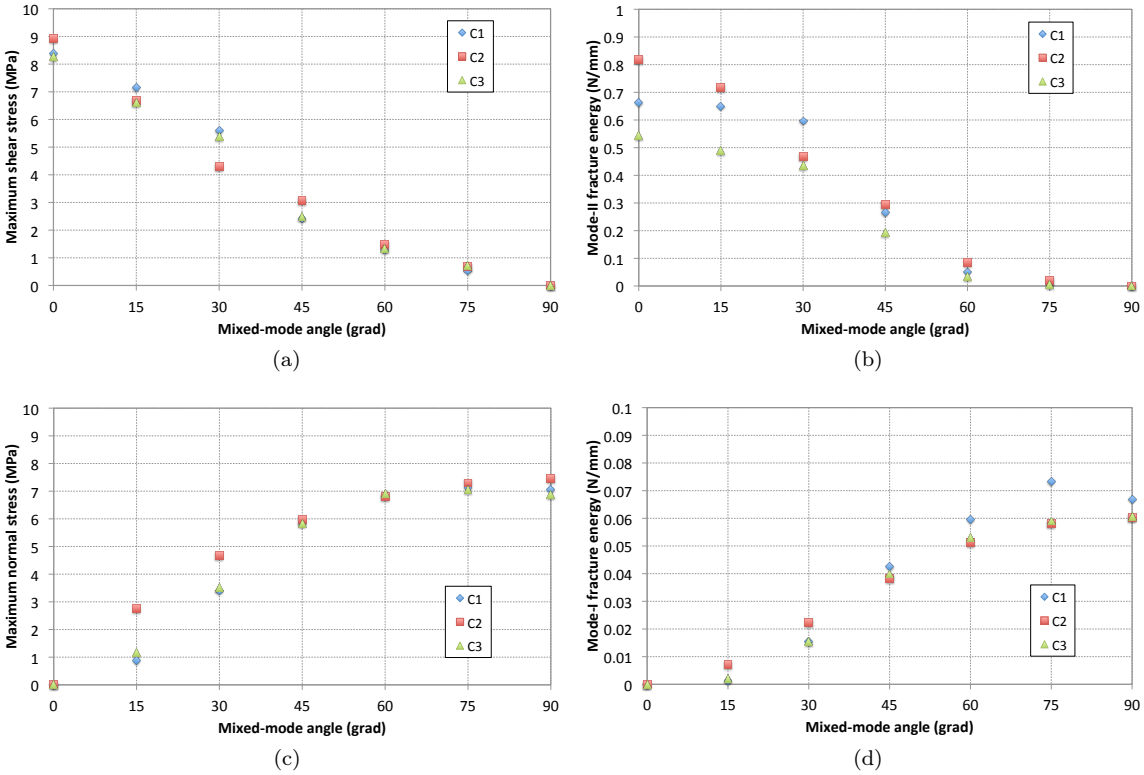


Figure 16: Mode-II cohesive strength (a) and fracture energy (b), mode-I cohesive strength (c) and fracture energy (d) as functions of the mixed-mode angle.

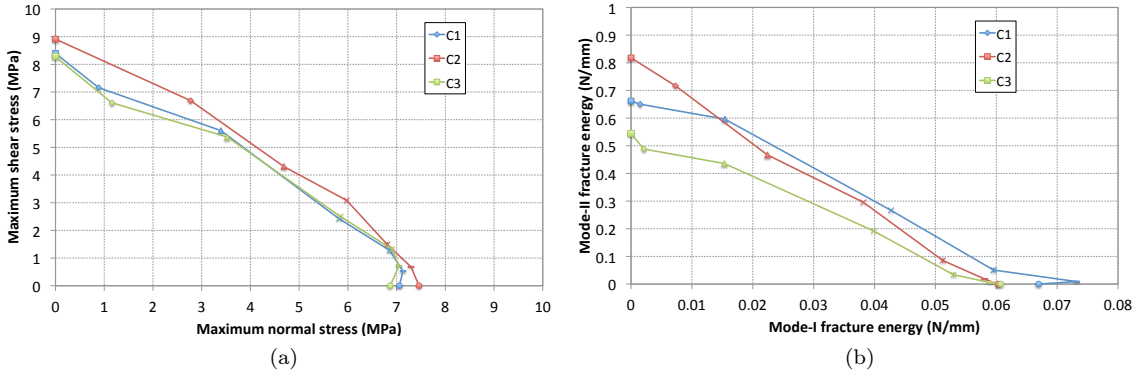


Figure 17: Mixed-mode cohesive strength (a) and fracture energy (b) failure envelopes.

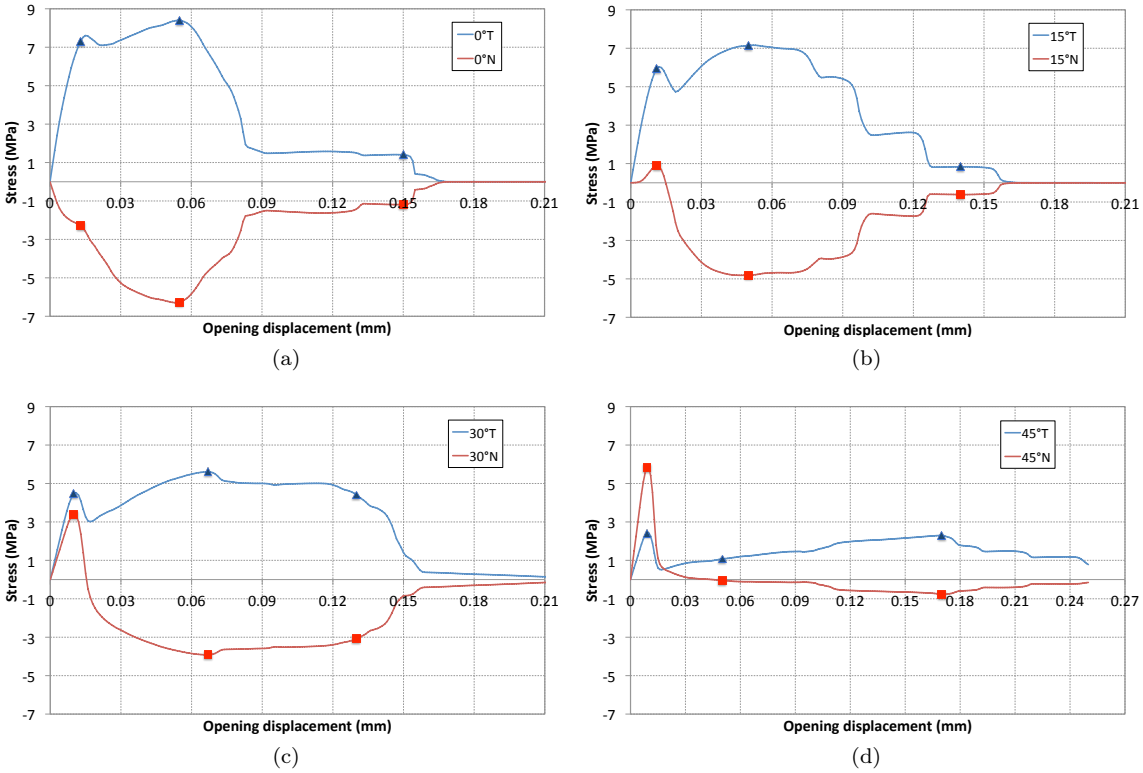


Figure 18: Mixed-mode cohesive behavior. Tangential (T) and normal (N) stresses vs. total opening displacement for one of the numerical tests for a mixed-mode angle of 0° (a), 15° (b), 30° (c), 45° (d).

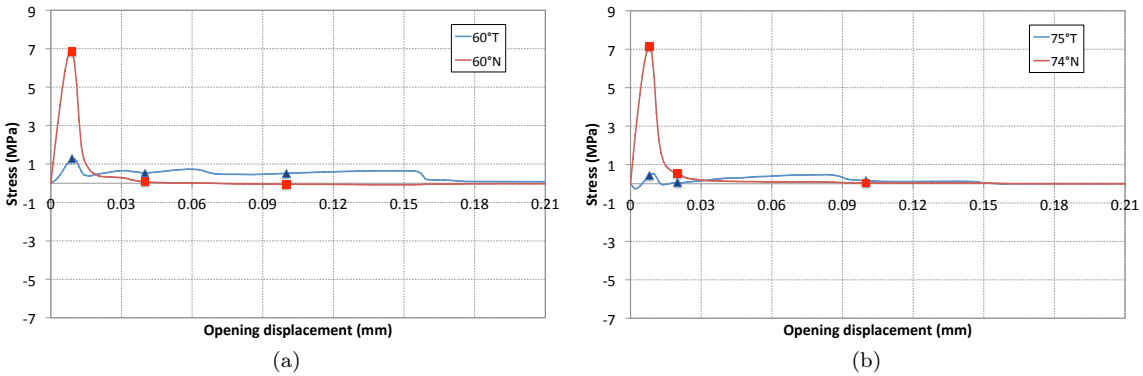


Figure 19: Mixed-mode cohesive behavior. Tangential (T) and normal (N) stresses vs. total opening displacement for one of the numerical tests for a mixed-mode angle of 60° (a), 75° (b), and 90° (c).

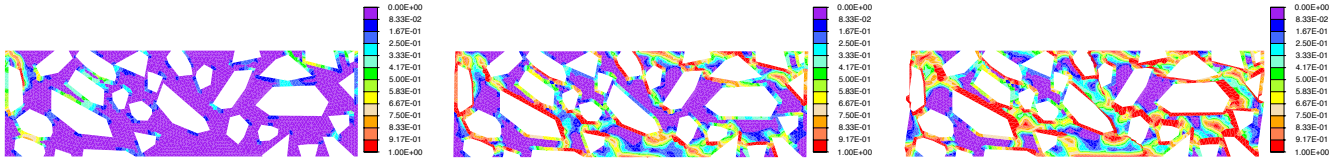


Figure 20: Damage variable distribution within the concrete sample under loading at a mixed-mode angle of 0° (pure mode II) at the stages of loading indicated with the markers in Figure 18a.

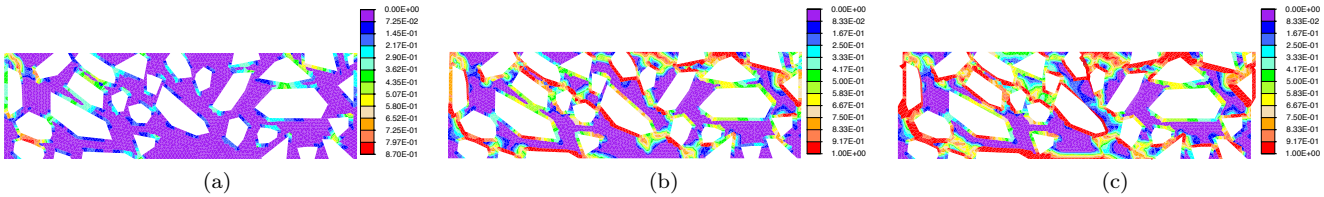


Figure 21: Damage variable distribution within the concrete sample under loading at a mixed-mode angle of 15° at the stages of loading indicated with the markers in Figure 18b.

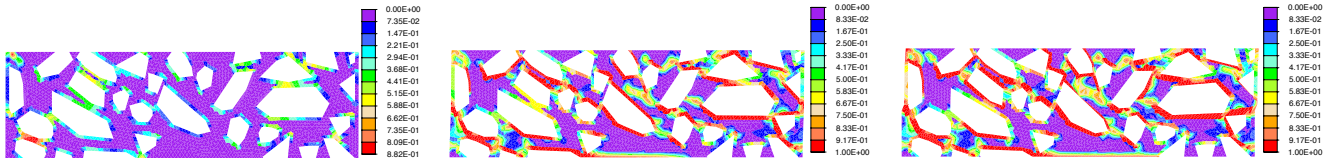


(a) (b) (c)

Figure 22: Damage variable distribution within the concrete sample under loading at a mixed-mode angle of 30° at the stages of loading indicated with the markers in Figure 18c.

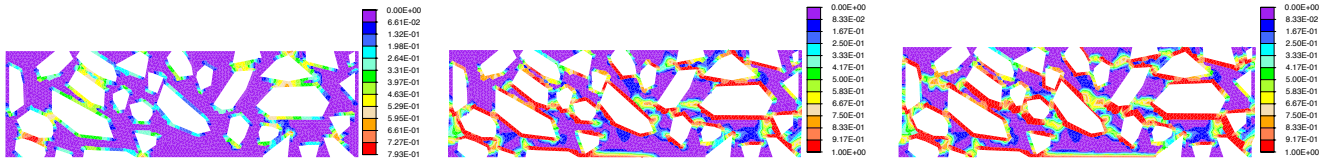


(a) (b) (c)

Figure 23: Damage variable distribution within the concrete sample under loading at a mixed-mode angle of 45° at the stages of loading indicated with the markers in Figure 18d.

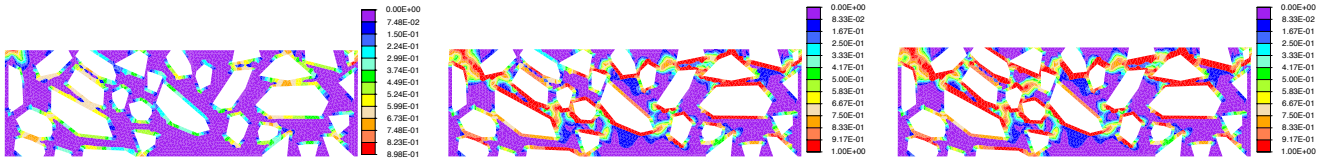


(a) (b) (c)

Figure 24: Damage variable distribution within the concrete sample under loading at a mixed-mode angle of 60° at the stages of loading indicated with the markers in Figure 19a.

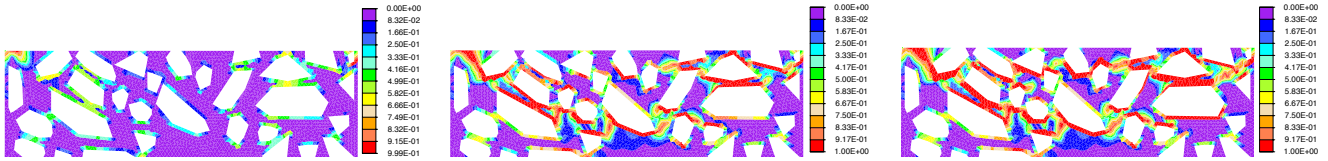


(a) (b) (c)

Figure 25: Damage variable distribution within the concrete sample under loading at a mixed-mode angle of 75° at the stages of loading indicated with the markers in Figure 19b.

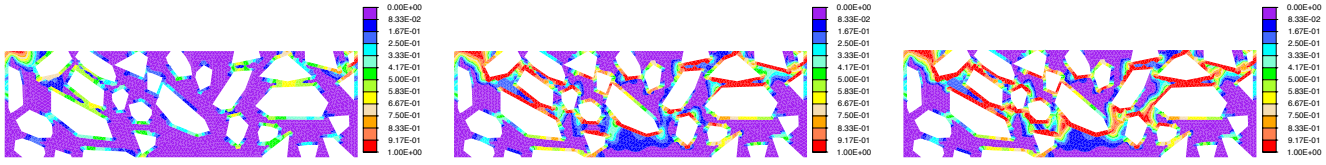


(a) (b) (c)

Figure 26: Damage variable distribution within the concrete sample under loading at a mixed-mode angle of 90° (pure mode I) at the stages of loading indicated with the markers in Figure 19c.

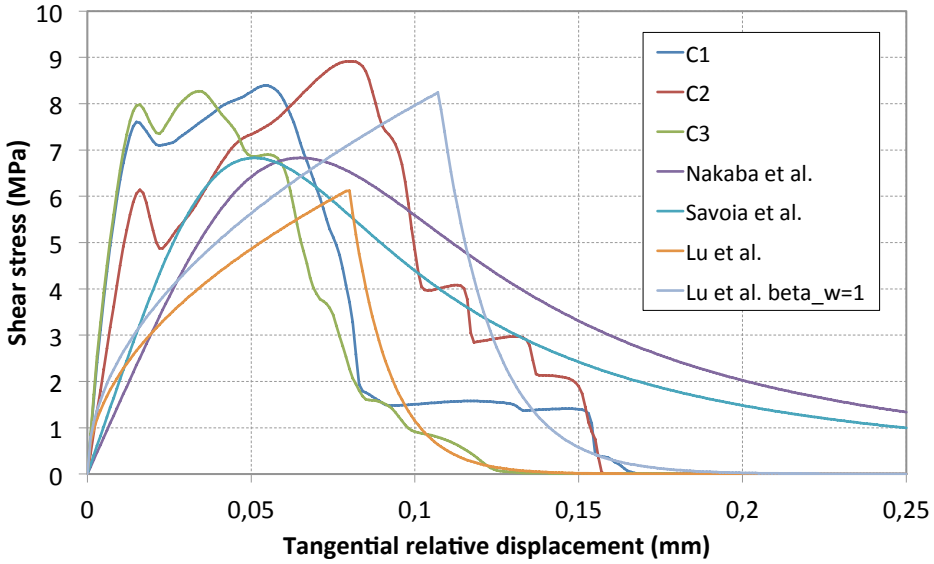


Figure 27: Comparison between mesomechanically-derived and analytical mode-II CZ laws.

## AppendixA. Derivation of the macroscopic interfacial traction

Invoking Eq. (24) and the displacement decomposition (25), Eq. (33) can be rewritten as

$$\overline{\delta W^m} = \frac{1}{w}\int_{\Gamma_t^m} \hat{\mathbf{t}}^m \cdot \boldsymbol{\delta}\mathbf{u}^m d\Gamma_t^m = \frac{1}{w}\left(\int_{\Gamma_t^m} \hat{\mathbf{t}}^m \cdot \boldsymbol{\delta}\mathbf{u}^M d\Gamma_t^m + \int_{\Gamma_t^m} \hat{\mathbf{t}}^m \cdot \boldsymbol{\delta}\tilde{\mathbf{u}} d\Gamma_t^m\right) \tag{A.1}$$

The first integral term in the right-hand side of Eq. (A.1) is developed as

$$\begin{aligned}\int_{\Gamma_t^m} \hat{\mathbf{t}}^m \cdot \boldsymbol{\delta}\mathbf{u}^M d\Gamma_t^m &= \int_{\Gamma_L^m} \hat{\mathbf{t}}^{m,L} \cdot \boldsymbol{\delta}\mathbf{u}^{M,L} d\Gamma_L^m + \int_{\Gamma_R^m} \hat{\mathbf{t}}^{m,R} \cdot \boldsymbol{\delta}\mathbf{u}^{M,R} d\Gamma_R^m + \\ &+ \int_{\Gamma_T^m} \hat{\mathbf{t}}^{m,T} \cdot \boldsymbol{\delta}\mathbf{u}^{M,T} d\Gamma_T^m + \int_{\Gamma_B^m} \hat{\mathbf{t}}^{m,B} \cdot \boldsymbol{\delta}\mathbf{u}^{M,B} d\Gamma_B^m \qquad \text{(A.2)} \\ &= \int_{\Gamma_R^m} \hat{\mathbf{t}}^{m,R} \cdot \left(\boldsymbol{\delta}\mathbf{u}^{M,R} - \boldsymbol{\delta}\mathbf{u}^{M,L}\right) ds_2 + \\ &+ \int_{\Gamma_T^m} \hat{\mathbf{t}}^{m,T} \cdot \boldsymbol{\delta}\mathbf{u}^{M,T} d\Gamma_T^m + \int_{\Gamma_B^m} \hat{\mathbf{t}}^{m,B} \cdot \boldsymbol{\delta}\mathbf{u}^{M,B} d\Gamma_B^m \qquad \text{(A.3)}\end{aligned}$$

$$
\begin{aligned}
&= \left(\boldsymbol{\delta u}^2 - \boldsymbol{\delta u}^1\right) \cdot \int_{\Gamma_R^m} \hat{\mathbf{t}}^{m,R} ds_2 + \boldsymbol{\delta u}^4 \cdot \int_{\Gamma_T^m} \hat{\mathbf{t}}^{m,T} ds_1 + \boldsymbol{\delta u}^1 \cdot \int_{\Gamma_B^m} \hat{\mathbf{t}}^{m,B} ds_1 \\
&= \boldsymbol{\delta u}^4 \cdot \int_{\Gamma_T^m} \hat{\mathbf{t}}^{m,T} ds_1 \qquad \text{(A.4)}
\end{aligned}
$$

where first the periodicity conditions given by Eqs. (29) and then the boundary conditions of the mesoscale RVE $\boldsymbol{\delta u}^1 = \boldsymbol{\delta u}^2 = \mathbf{0}$ have been used. The second integral term on the right-hand side of Eq. (A.1) can be developed as

$$
\begin{aligned}
\int_{\Gamma_t^m} \hat{\mathbf{t}}^m \cdot \boldsymbol{\delta \tilde{u}} d\Gamma_t^m &= \int_{\Gamma_L^m} \hat{\mathbf{t}}^{m,L} \cdot \boldsymbol{\delta \tilde{u}}^L d\Gamma_L^m + \int_{\Gamma_R^m} \hat{\mathbf{t}}^{m,R} \cdot \boldsymbol{\delta \tilde{u}}^R d\Gamma_R^m + \int_{\Gamma_T^m} \hat{\mathbf{t}}^{m,T} \cdot \boldsymbol{\delta \tilde{u}}^T d\Gamma_T^m + \int_{\Gamma_B^m} \hat{\mathbf{t}}^{m,B} \cdot \boldsymbol{\delta \tilde{u}}^B d\Gamma_B^m \\
&= \int_{\Gamma_R^m} \hat{\mathbf{t}}^{m,R} \cdot \left(\boldsymbol{\delta \tilde{u}}^R - \boldsymbol{\delta \tilde{u}}^L\right) ds_2 + \int_{\Gamma_T^m} \hat{\mathbf{t}}^{m,T} \cdot \boldsymbol{\delta \tilde{u}}^T ds_1 + \int_{\Gamma_B^m} \hat{\mathbf{t}}^{m,B} \cdot \boldsymbol{\delta \tilde{u}}^B ds_1 \\
&= 0 \qquad \text{(A.5)}
\end{aligned}
$$

where the boundary conditions Eq. (27-28) are used. Inserting Eqs. (A.4) and (A.5) into Eq. (A.1) gives

$$
\overline{\delta W^m} = \frac{1}{w} \boldsymbol{\delta u}^4 \cdot \int_{\Gamma_T^m} \hat{\mathbf{t}}^{m,T} d\Gamma_t^m \qquad \text{(A.6)}
$$

Substituting Eqs. (32) and (A.6) into (31) leads to

$$
\mathbf{t}^M = \frac{1}{w} \int_{\Gamma_T^m} \hat{\mathbf{t}}^{m,T} d\Gamma_t^m \qquad \text{(A.7)}
$$